Gas Dynamics and Kinetics in the Cometary Coma: Theory and Observations

Michael R. Combi
University of Michigan

Walter M. Harris
University of Washington

William H. Smyth
Atmospheric & Environmental Research, Inc.

Our ability to describe the physical state of the expanding coma affects fundamental areas of cometary study both directly and indirectly. In order to convert measured abundances of gas species in the coma to gas production rates, models for the distribution and kinematics of gas species in the coma are required. Conversely, many different types of observations, together with laboratory data and theory, are still required to determine coma model attributes and parameters. Accurate relative and absolute gas production rates and their variations with time and from comet to comet are crucial to our basic understanding of the composition and structure of cometary nuclei and their place in the solar system. We review the gas dynamics and kinetics of cometary comae from both theoretical and observational perspectives, which are important for understanding the wide variety of physical conditions that are encountered.

1. INTRODUCTION

Gases, primarily water, and entrained dust are liberated from the icy nucleus by solar heating when a comet is within a few astronomical units (AU) of the Sun and form an outflowing cometary atmosphere. The cometary atmosphere, or coma, expands to distances many orders of magnitude larger than the size of the nucleus itself. Because of the ultimate expansion into vacuum and the very weak gravity that affects only the largest dust particles, a Knudsen layer of a fraction to a few meters in thickness (a few times the molecular collision mean free path) forms near the surface where the gas organizes itself into a transient stationary thermal layer. The initiation of regular flow transforms this thermal layer into a rapid transonic dusty-gas flow with a typical scale length of 10–100 m. Expansion and nearly adiabatic cooling dominates the flow out to scales of ~100 km where the dust becomes decoupled collisionally from the gas. Here the gas flows with a speed of ~700 m s^{-1} and has a cool temperature of <30 K. The energetic photochemical products of solar UV photodissociation then begin to heat the gas faster than it can cool by adiabatic expansion or IR radiational cooling, and the gas kinetic temperature and ultimately the outflow speed increase. Photoionization and charge impact ionization (~5–10% of the photodissociation rate) forms a cometary ionosphere on scales of 10^3–10^4 km, which ultimately interacts with the magnetized plasma of the solar wind forming an ion tail on scales of 10^5–10^7 km. Also, at large scales of 10^6–10^7 km, the neutral coma is broken down into its atomic constituents, such as O, H, C, and N. This description is most applicable for a typical comet observed in the range of a few tenths to about 2 AU from the Sun. For comets much farther away, temperatures and velocities are smaller and reaction length scales are larger. And for comets much closer (Sun-grazers), temperatures and velocities are much larger and reaction length scales are smaller.

Our understanding of the conditions within a few times the radius of the nucleus results largely from model predictions that are only constrained by the gas fluxes and velocities hundreds of nucleus-radii from the nucleus, and are determined both by *in situ* and remote observations. There are not many direct observations about the conditions near the surface, beyond the images of 1P/Halley from the *Giotto* and *Vega* spacecrafts and those of 19P/Borrelly from the *Deep Space 1* spacecraft, which show only the dust distribution. This region is described in detail in *Crifo et al.* (2004). The photodissociation, photoionization and fast ion-neutral chemical reactions involving ultimately ~100 species and thousands of reactions forms a complex atmosphere/ionosphere that is described in detail in *Rodgers et al.* (2004).

The region of the coma accessible by remote ground-based and Earth-orbit-based observations and by direct *in situ* sampling by spacecraft instrumentations (mostly by neutral gas and plasma mass spectrometers) for detailed study generally covers distances larger than a few hundred kilometers from the nucleus. Remote imaging observations of this region have provided information about the projected line-of-sight-integrated distribution of neutral gas and ion

species in two spatial dimensions on the sky plane and sometimes the line-of-sight velocity distribution. Thus remote sensing provides somewhat convoluted, nonunique, global views of the coma, whereas *in situ* measurements have provided some detailed information about neutral gas and ion densities, velocities, and temperatures, but only for a few fleeting threads along a few spacecraft trajectories. Information about kinetic and rotational temperatures has been obtained by both remote observations and *in situ* measurements. The spectroscopic measurements are discussed in detail in *Bockelée-Morvan et al.* (2004) (for parent species) and *Feldman et al.* (2004) (for nonparent species).

It is important to understand the physical state of the coma and its variations because it is largely from analyses of observations of various species in the coma that we determine the composition of the larger population of comets. Although in the last 20 years IR and radio astronomy have opened the possibility of directly observing parent gas species in comets, interpreting these observations is complicated by difficult excitation mechanisms, atmospheric extinction (in the IR), and generally weaker signal-to-noise when compared with visible and near-UV measurements of daughter species. The interpretations of measurements of daughter species have their own sets of complicating issues regarding production models and kinematics. However, routine observations of daughter species in the visible remains critically important for the foreseeable future because they are more sensitive for weak comets and especially for those at large heliocentric distances. This is the only practical way to characterize the composition and activity of the entire population of comets and to compare with the large base of existent data. Observations of daughter species in the visible should also be made and interpreted side-by-side with IR and radio observations of parent species for brighter comets and those at generally smaller heliocentric distances to enable the entire complex picture to be unraveled.

In this chapter we concentrate on those aspects of photochemistry and dynamics that are important for understanding the overall physical state of the coma, and their variations from comet to comet, with changing heliocentric and cometocentric distance, and, most importantly, in the region sampled by observations, i.e., outside a few hundred kilometers from the nucleus. We also discuss quantitative models of the coma beginning with the original fountain model of *Eddington* (1910), which started the heuristic approach continued by *Haser*'s (1957) model that in turn later treated the coma as a free expansion problem including production and loss processes. From there we move to physics-based models that treat the energy budget, dynamics, and chemistry, leading to hydrodynamics, kinetic and hybrid models. These models provide the basis for interpreting and linking together multiple diagnostic observations of comets that are becoming increasingly precise. Care must be taken in interpreting observations either using complex models with too many free (and especially unconstrained) parameters, or using simple models with mathematically constrained parameters, where their direct physical meaning may be simplistic or inaccurate.

2. FREE-EXPANSION MODELS

2.1. Eddington to Wallace and Miller Fountain Models

In Eddington's fountain model the comet is assumed to be a uniform and isotropic point source of emitters of light such that their density (e.g., gas or dust) would fall as the inverse square of the distance from the source, except the emitters are also subject to a uniform acceleration that pushes on them from a given direction (presumably from the Sun's direction). Eddington showed that such a model defines a paraboloid of revolution along a line parallel to the acceleration and passing through the point source (the nucleus of the comet) such that

$$x^2 + y^2 = 2z\,\frac{v^2}{a} + \frac{v^4}{a^2} \qquad (1)$$

where the acceleration, a, is directed in the +z direction, x and y complete the righthanded Cartesian coordinates, and v is the initial uniform outflow speed of the emitting particles. In this case the density, n, of emitting particles is determined by two trajectories that cross any given point within the paraboloid. Later work by *Mocknatsche* (1938), which was independently rediscovered by *Fokker* (1953) and later described by *Wallace and Miller* (1958), showed that the column density, which is what would be observed by a remote observer through an optically thin paraboloid of such particles, N, can be calculated after some algebraic manipulation for any line-of-sight that passes within the projected paraboloid for any angle between the Sun, comet, and observer to simply be

$$N = \frac{Q}{4vR} \qquad (2)$$

where Q is the global particle production rate and R is the projected distance on the "sky" plane from the source (i.e., the nucleus). Interestingly, this is the same result as for a point source without the acceleration. The projected shape of the paraboloid, of course, depends on the viewing geometry. Such a model is still used to understand many basic properties of the observed dust distribution in comets.

2.2. *Haser* (1957) Model

Most radiative emissions of gaseous species in comets in visible light are caused by fluorescence with sunlight through an otherwise practically optically thin medium. Early quantitative observations of gas species in the cometary coma indicated that the spatial variation of the observed brightness of some emissions (e.g., C_2, CN, etc.) deviated from the simple inverse distance relation of a simple fountain model. It was also realized that most of the gas species observed and identified through visible range spectroscopy were not stable molecules but unstable radicals that could be stored in an otherwise icy nucleus but were more likely produced in the photodissociation of parent molecules by solar UV radiation. In order to describe

the kind of expected distribution of an observed gaseous species in the coma of a comet, one needs to account (potentially) for the creation of that species from a parent species and its destruction into some simpler species. An example would be the production of observed OH by photodissociation of H_2O and the subsequent photodissociation of the OH into O + H.

The quantitative description of this was put forth by *Haser* (1957) in a now classic formulation that is still widely used today. Haser considered the distribution of a secondary species (like some cometary radical) being produced by the photodissociation of some parent molecule and in turn being destroyed by some photodestruction process. If the coma is considered to be a spherically symmetric point source of uniformly outflowing parent molecules, where an exponential lifetime describes its destruction, then the density, n_p, of parents at some distance from the point source, r, is given by

$$n_p(r) = \frac{Q}{4\pi r^2 v}(e^{-r/\gamma_p})$$

The density, n_d, of a daughter species created by the destruction of these parents is given by

$$n_d(r) = \frac{Q}{4\pi r^2 v}\frac{\gamma_d}{\gamma_p - \gamma_d}(e^{-r/\gamma_p} - e^{-r/\gamma_d}) \qquad (3)$$

where r is the distance from the nucleus, and γ_p and γ_d are the parent and daughter scale lengths given by the product of the radial outflow speed, v, and exponential lifetimes of the parent of the observed species, τ_p, and that of the observed daughter species, τ_d, itself, respectively. The model is most often used with observed intensity spatial profiles, which are typically proportional to the column density profile of the emitting species. Therefore, normally equation (3) is integrated along the line-of-sight. This can either be performed numerically or written in the form of modified Bessel function as done originally by Haser, which yields

$$N_d(\rho) = \frac{Q}{2\pi\rho v}\frac{\gamma_d}{\gamma_p - \gamma_d}\left(\int_0^{\rho/\gamma_p} K_0(y)dy - \int_0^{\rho/\gamma_d} K_0(y)dy\right) \qquad (4)$$

where ρ is the projected distance from the nucleus through which the line-of-sight integration is performed and $K_0(y)$ is the modified Bessel function of the first kind.

Figure 1 (*Combi and Fink,* 1997) shows the range of the family of column density spatial profiles possible with Haser's model. An interesting, but little mentioned, attribute of this equation is that the spatial profile shape is the same if the parent and daughter scale lengths are interchanged, yielding simply an extra factor of the ratio of the two scale lengths. This means that it is not possible to say whether the parent or daughter scale length is the smaller based only on an observation of the daughter spatial profile.

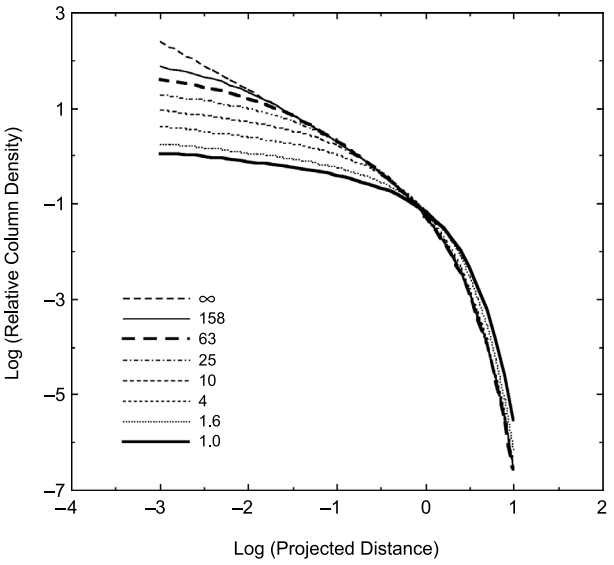

Fig. 1. Family of Haser model profiles of daughter species column densities for different values of the ratio of the scale lengths plotted as a function of projected distance in units of the daughter scale length. Note that a scale length ratio of infinity (∞) corresponds to a parent molecule distribution.

2.3. Models with Secondary Product Velocities

Of the several simplifying assumptions of Haser's model as most often used, which include spherical symmetry, constant outflow velocity, and steady-state gas production, one of the basic assumptions is that both the parent and daughter products undergo purely radial motion. Early results of UV observations of comets indicated that H and OH were produced by photodissociation of water and that this would lead to nonnegligible excess energy, which would be distributed in the form of superthermal velocities for the daughter products. The large speeds of the H atoms imply velocities for the heavier products in the photodissociation network, namely O and OH, in the range of 1–2 km s^{-1}. These are generally larger than the outflow speed of the parent molecules in the coma itself and therefore posed a serious violation of the assumption of radial outflow for daughter species in Haser's model. However, the use of Haser's model for interpreting spatial profiles of column density derived from brightness observations already required either integrals of modified Bessel functions (equation (4)) or direct numerical integration of the density function (equation (3)) itself. The addition of nonradial ejection of daughter species yields a nonanalytical integral for the density function itself.

Festou (1981a) and *Combi and Delsemme* (1980) addressed solving this problem in two different ways. *Festou* (1981a) introduced the vectorial model, which represented a numerical approach to directly solving for the density and column density distribution. *Combi and Delsemme* (1980) introduced Monte Carlo techniques, developed originally for nuclear reactor particle transport and radiative transfer

calculations, to simulate the expansion. In their more modern versions, the vectorial model is faster computationally, but the Monte Carlo technique is directly applicable to even more general problems, such as variable outflow velocity, aspherical comae, and radiation pressure acceleration of the daughter species.

The main effect of the ejection of daughter species on observed spatial profiles is that profiles produced are not related to those using Haser's model with scale lengths simply given by the velocities × the lifetimes. These more complicated models did, however, account for the fact that most prospective parent molecule lifetimes were actually longer than the Haser model parent scale length would indicate, given a reasonable assumption for the parent velocity.

Combi and Delsemme (1980) also introduced what started as a heuristic geometrical argument for relating the given velocities and lifetimes that would give a realistic spatial profile with the vectorial model (or Monte Carlo simulation) to a Haser model with some set of Haser scale lengths. This so-called "average random walk model" specifies transformations from the actual parent and daughter velocities and lifetimes to the equivalent Haser-model scale lengths. Also, like the typically used vectorial model and first Monte Carlo models, this assumes the coma is collisionless for the daughter products. In the case of a highly collisional coma, the ejection velocity will be collisionally quenched; however, in this case, another simplification of the Haser model, a constant radial outflow speed, will most certainly be violated. Such was the case for C/1995 O1 Hale-Bopp (*Combi,* 2002). If v_p and v_e are the parent outflow and daughter ejection velocities, respectively, and τ_p and τ_d are the parent and daughter lifetimes, respectively, then the Haser equivalent parent and daughter scale lengths, γ_{pH} and γ_{dH}, can be calculated from the following set of relationships. If we make the definitions that

$$\tan\delta \equiv \frac{v_p}{v_e} \quad \mu \equiv \frac{\gamma_p}{\gamma_d} \quad \mu_H \equiv \frac{\gamma_{pH}}{\gamma_{dH}}$$

where $\gamma_p = v_p\tau_p$ and $\gamma_d = v_d\tau_d$, $v_d = (v_p^2 + v_e^2)^{1/2}$ and v_e is the isotropic ejection velocity of the daughter upon production with respect to the original center-of-mass of the parent. The equations (5)–(7) can be used to go back and forth between the vectorial values and the Haser equivalent scale lengths for a given ratio of the parent outflow to daughter ejection velocity.

$$\gamma_d^2 - \gamma_p^2 = \gamma_{pH}^2 - \gamma_{dH}^2 \tag{5}$$

$$\mu_H = \left(\frac{\mu + \sin\delta}{1 + \mu\sin\delta}\right)\mu \tag{6}$$

or equivalently

$$\mu = (\mu_H - 1)\frac{\sin\delta}{2}\left[(\mu_H - 1)^2\,\frac{\sin^2\delta}{4} + \mu_H\right]^{1/2} \tag{7}$$

In order to complete the substitution in the density or column density expressions for Haser's model, the effective radial velocity, v, in the denominators in the first terms on the righthand sides of equations (3) and (4) must be the Haser equivalent daughter expansion velocity v_{dH}, given as

$$v_{dH} = v_d\frac{\gamma_{dH}}{\gamma_d} \tag{8}$$

2.4. Three-Generation Haser-like and Monte Carlo Models

Observations of spatial profiles of cometary C_2 have often had some difficulty in being interpreted either with a simple two-generation Haser model or with a model accounting for secondary product ejection velocities (see *Feldman et al.,* 2004). The problem is that the innermost part of the profile has often been seen to be even flatter than is possible to be reproduced using any Haser model. A Haser model that has the flattest inner profile (see Fig. 1) is one in which the parent and daughter scale lengths are equal. Models that allow for secondary product velocities actually exacerbate the problem, because the effect of isotropic ejection of daughters makes the radial parent scale length seem to be shorter, thus making the profile look like Haser models with unequal scale lengths.

Observations of C_2 in Comet Halley (*O'Dell et al.,* 1988; *Wyckoff et al.,* 1988; *Fink et al.,* 1991) were noteworthy in showing the flattening of the inner profile. *Fink et al.* (1991) chose to use the standard two-generation Haser model but fitted models with equal parent and daughter scale lengths. *Wyckoff et al.* (1988) suggested that either C_2 was produced as a granddaughter species or by grains instead of simple photodissociation. These had been suggested much earlier by both *Jackson* (1976) and *Cochran* (1985). *O'Dell et al.* (1988) pursued the granddaughter species idea by performing model calculations for a three-generation Haser-type model, generalizing the earlier work of *Yamamoto* (1981) and *Festou* (1981a), who applied a three-generation Haser-type model to comet-centered, circular aperture observations.

The three-generation Haser-type model yields an expression for the column density profile that was given by *O'Dell et al.* (1988) as

$$N(\rho) = \frac{Q_1}{2\pi V_3\rho}[AH(\beta_1\rho) + BH(\beta_2\rho) + CH(\beta_3\rho)] \tag{9}$$

where Q_1 is the global production rate of the observed (granddaughter) species; V_3 is its radial expansion velocity; and β_1, β_2, and β_3 are the inverse scale lengths of the original parent, the intermediate daughter, and the observed granddaughter species, respectively. The quantities A, B, and C are given as

$$A = \frac{\beta_1\beta_2}{[(\beta_1 - \beta_2)(\beta_1 - \beta_3)]} \qquad B = \frac{-A(\beta_1 - \beta_3)}{(\beta_2 - \beta_3)}$$

$$C = \frac{-B(\beta_1 - \beta_2)}{(\beta_1 - \beta_3)}$$

The function H(x) is given by

$$H(x) = \frac{\pi}{2} - \int_0^x K_0(y)dy$$

where $K_0(y)$ is again the zero-order modified Bessel function of the second kind.

One of the simplifications of this model is the same as in the two-generation model of *Haser* (1957), i.e., that at each step the daughter and granddaughter species are assumed to continue to travel in a purely radial direction. *Combi and Fink* (1997) addressed this by using Monte Carlo techniques to explore models that include ejection velocities for the dissociation product at either or both dissociation steps. This was done for the purpose of putting limits on prospective original parents of observed C_2, but would also explain the flat inner profile. Figure 2 shows one of their figures showing comparisons of four otherwise comparable models: (1) a two-generation Haser model where the parent and daughter scale lengths are equal (this one gives the flattest possible inner profile); (2) a Monte Carlo simulation of a three-generation model that is otherwise similar to that which could be produced using equation (12) of *O'Dell et al.* (1988) and could, as they showed, give a reasonable reproduction of the spatial profile of C_2 in Comet 1P/Halley, (3) a Monte Carlo simulation of a three-generation model where the ejection velocity of the product at each dissociation equals half of the parent outflow velocity; and (4) a similar model but where both ejection velocities are equal to the parent velocity. They also provided other sets of comparisons. The result was that the addition of daughter and granddaughter ejection velocities causes three-generation models to be unable to produce flat inner profiles, and makes them essentially similar to some two-generation Haser or vectorial model with different parameters. Conversely for C_2, the results implied that if C_2 is a third-generation species, then the total of the ejection velocities for each dissociation step had to be less than about half the parent outflow velocity. In typical photodissociations there are 2–4 eV of excess energy that would impart an ejection velocity of 1 km s^{-1} or more to the heavier dissociation product that would contain C_2, or C_2 itself.

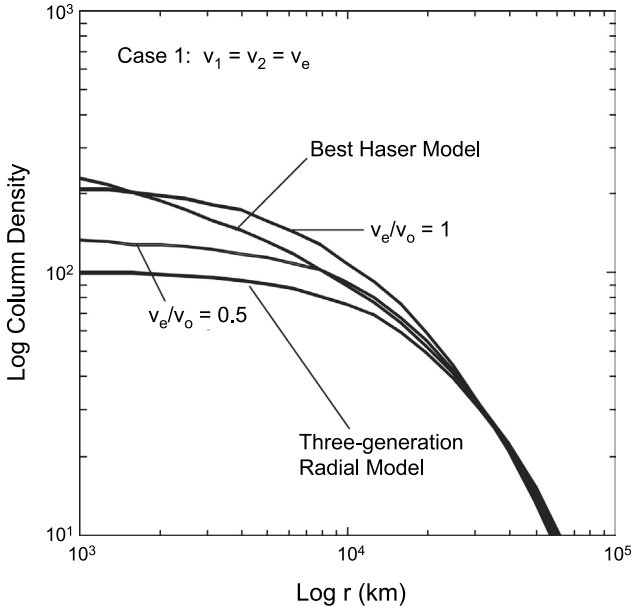

Fig. 2. Haser and three-generation model spatial profiles with non-zero daughter ejection speeds. Case 1 from *Combi and Fink* (1997) compares a general three-generation dissociation model with ejection speeds at each dissociation. The two ejection speeds are equal to each other and either equal to the parent outflow speed, v_0, or to half of it. The three-generation radial model is one where there is zero ejection speed for the photodissociation products at either step. The "Best Haser Model" is one where the daughter and parent scale lengths are equal, which results in the flattest inner profile that is most like the observed inner profile of C_2 in Comet 1P/Halley. When the daughter ejection speed is nonnegligible, a three-generation model does not produce a flat inner profile.

2.5. Grains as Gas Sources

Volatile grains have been suggested as possible sources for observed species in comets for a long time (see review by *Festou,* 1999). The idea regained new interest with the discovery of CN and C_2 jets in Comet 1P/Halley (*A'Hearn et al.,* 1986) and extended sources for CO and H_2CO (*Eberhardt et al.,* 1987; *Meier et al.,* 1993; *DiSanti et al.,* 2001), and from observations of a substantial distributed icy grain source from C/1996 B2 (Hyakutake) (*Harris et al.,* 1997; *Harmon et al.,* 1997). *Delsemme and Miller* (1971) presented a model calculation for the production of an observed gas from grains, analogous to the two-generation model of *Haser* (1957), except where evaporating grains serve as the parent of the observed species rather than photodissociating parent molecules.

This model, however, suffers from the same limitation as Haser's model, which is that the observed daughter species is restricted to perfectly radial motion. Clearly molecules released from evaporating grains would have some nonnegligible velocity owing to the temperature of the grains. The effect would be even more important if the grains were dark organic-rich CHON grains, which are expected to reach and sublimate at temperatures higher than the blackbody temperature for some given distance from the Sun (*Lamy and Perrin,* 1988). This temperature would generally be much higher than the sublimation temperature of water for heliocentric distances less than about 3 AU. *Combi and Fink* (1997) introduced a CHON grain halo model for gas species that generalizes the icy grain halo model of *Delsemme and Miller* (1971) in the same way as the vectorial (*Festou,* 1981a) and Monte Carlo (*Combi and Delsemme,* 1980) models generalized Haser's model, i.e., by allowing for isotropic ejection of the daughter species

TABLE 1. Photochemical branching and exothermic velocities for H_2O vapor.

Solar Ultraviolet Wavelength Range	Reaction	Product Exothermic Velocities (km s^{-1})		Photodestruction Rate* (10^{-6} s^{-1}) [*Branching Ratio*] (Quiet Sun)	(Active Sun)
1357–1860 Å	$H_2O + h\nu \rightarrow H + OH(X^2\Pi)$	18.5 (H)†	1.09 (OH)†	4.84 [*0.465*]	5.36 [*0.380*]
	$\rightarrow H_2 + O(^1D)$	<13.7 (H_2)	<1.71 (O)	0.05 [*0.005*]	0.05 [*0.004*]
1216 Å	$H_2O + h\nu \rightarrow H + OH(X^2\Pi)$	17.2 (H)†	1.01 (OH)†	3.02 [*0.291*]	4.53 [*0.321*]
	$\rightarrow H + OH(A^2\Sigma^+)$	5 (H)‡	0.3 (OH)‡	0.35 [*0.033*]	0.52 [*0.037*]
	$\rightarrow H_2 + O(^1D)$	<15 (H_2)‡	<1.8 (O)‡	0.43 [*0.042*]	0.65 [*0.046*]
	$\rightarrow H + O + H$	<7.4 (2H)§	<0.87 (O)§	0.52 [*0.050*]	0.78 [*0.055*]
984–1357 Å (excluding 1216 Å)	$H_2O + h\nu \rightarrow H + OH(X^2\Pi)$	<37–27 (H)¶,**	<2.2–1.6 (OH)¶,**	0.30 [*0.028*]	0.45 [*0.032*]
	$\rightarrow H + OH(A^2\Sigma^+)$	<25–0 (H)**	<1.5–0 (OH)**	0.03 [*0.003*]	0.05 [*0.004*]
	$\rightarrow H_2 + O(^1D)$	<22–14 (H_2)**	<2.7–1.7 (O)**	0.04 [*0.004*]	0.07 [*0.005*]
	$\rightarrow H + O + H$	<17–0 (2H)**	<2.0–0 (O)**	0.05 [*0.005*]	0.08 [*0.005*]
<984 Å	$H_2O + h\nu \rightarrow$ neutral products	—	—	0.25 [*0.024*]	0.41 [*0.029*]
	$\rightarrow$ ionization products	—	—	0.52 [*0.050*]	1.16 [*0.082*]
Total:				10.40 [*1.000*]	14.11 [*1.000*]

* From S. A. Budzien (personal communication, 2003); updated and slightly different than *Budzien et al.* (1994).
† Average velocity from *Crovisier* (1989) and similar to *Wu and Chen* (1993).
‡ Average velocity from *Festou* (1981b).
§ Determined using the excess energy of 13 kcal $mole^{-1}$ from *Slanger and Black* (1982).
¶ Similar to the values of 35–25 (H) and 2.0–1.2 (OH) from *Festou* (1981b).
** Upper limits determined for the bounding lower and higher (or threshold) wavelengths.

from the radially outflowing parent grains (in this case). The flat inner profiles of cometary C_2 have been the main subjects of three-generation and grain-halo models, and can be reproduced by either three-generation or grain-source models with appropriate parameters (*Combi and Fink,* 1997).

3. WATER-DOMINATED OUTFLOW

Water dominates up to ~90% of the volatile species that outflow from the cometary nucleus within ~3–4 AU from the Sun. During this outflow, the H_2O parent molecule is destroyed primarily through photodissociation, and to a much smaller extent, through photoionization and also dissociation and ionization interactions with solar wind ions and electrons. The destruction of H_2O creates secondary or daughter molecular products, OH and H_2, atomic products, O and H, and various ion species in the inner and outer comet coma. The neutral product species are detected remotely through solar resonance fluorescence for OH and H and also through dissociative excitation for O. The dissociation rates of H_2O, OH, and H_2 and the imparted exothermic energy to their daughter products are of fundamental importance in determining the spatial decay rates of these parent and daughter species in the coma and in determining the basic background density and temperature structure for all species in the coma. The photodestruction rates of H_2O, OH, and H_2 are variable and depend upon the heliocentric distance and radial velocity of the comet as well as the wavelength-dependent short-term modulations and longer-term 11-year periodic variations in solar radiation.

3.1. Water Photochemistry

The photochemistry and photochemical kinetics for H_2O in comets have been studied in detail by a number of investigators (*Huebner and Carpenter,* 1979; *Openheimer and Downey,* 1980; *Festou,* 1981a,b; *Huebner,* 1985; *Krasnopolsky et al.,* 1986a,b; *Allen et al.,* 1987; *Crovisier,* 1989; *Huebner et al.,* 1992; *Wu and Chen,* 1993; *Cochran and Schleicher,* 1993; *Budzien et al.,* 1994). The calculated photodestruction rates for different products have become more accurately determined with time because of improvements in cross sections and in the description of the solar flux spectrum and its time variations, although a number of uncertainties still remain. A summary of the relevant photodestruction reactions, product exothermic velocities, reaction rates, and branching ratios for H_2O is given in Table 1 and is divided into four wavelength ranges.

The first wavelength range is bounded above by the effective onset wavelength at 1860 Å for a nonzero photoabsorption cross section, and below by the threshold wavelength at 1357 Å for which OH can be produced in excited electronic states. In this first wavelength range, the measured relative branching ratios of the rates for the first and

second reaction are 0.99 and 0.01 respectively (*Stief et al.,* 1975), where in the second reaction $O(^1D)$ is produced since the production of $O(^3P)$ is spin forbidden.

The second wavelength range is only for the large Lyman-α peak at 1216 Å in the solar spectrum. For the Lyman-α peak, the measured relative branching ratios of the rates for the four reactions are 0.70, 0.08, 0.1, and 0.12 respectively (*Slanger and Black,* 1982), where the geometry and mechanisms for the three-body dissociation in the fourth reaction are not known (see *Wu and Chen,* 1993).

The third wavelength range is from 1357 Å to the threshold wavelength at 984 Å for ionization of water and excludes the solar spectrum contribution of the Lyman-α peak. In the third wavelength range, the relative branching ratios for the four reactions are not well known and are assumed in Table 1 to be the same as for the Lyman-α wavelength.

The fourth wavelength range is below the ionization threshold at 984 Å and includes a contribution from a dissociation cross section with unknown neutral products and a contribution from an ionization cross section with a mix of ionized and not-well-defined neutral products. The cross section for photoionization becomes more important than that for photodissociation below ~875 Å (see *Wu and Chen,* 1993).

The H_2O photodestruction rates for the four wavelength ranges depend upon an accurate specification of the appropriate wavelength-dependent cross sections and the variable solar flux. The photodestruction rates adopted in Table 1 are for the most recent calculations of S. A. Budzien (personal communication, 2003), which are based upon updated information for the photodissociation cross section in the first wavelength range and the solar flux at 1 AU and provide improved rates that differ only slightly from those calculated earlier by *Budzien et al.* (1994). Depending upon quiet and active Sun conditions, the first wavelength range contributes ~47.0–38.4% of the total photodestruction rate, the Lyman-α solar spectra peak contributes ~41.6–45.9%, the third wavelength range contributes 4.0–4.6%, and the fourth wavelength range contributes 7.4–11.1%. The corresponding branching ratios for the individual reactions in the four wavelength intervals are also given and are determined by the relative branching ratios discussed earlier. The total photodestruction rate of H_2O has a value in Table 1 for quiet and active Sun conditions, respectively, of $1.04 \pm 0.123 \times 10^{-5}$ s^{-1} (lifetime ~0.96×10^5 s) and $1.411 \pm 0.175 \times 10^{-5}$ s^{-1} (lifetime ~0.71×10^5 s).

For the different wavelength ranges in Table 1, the product exothermic velocities depend upon the details of the photochemical kinetics and are distributed nonuniformly in discrete velocity groups that are constrained between 0 and 2.7 km s^{-1} for O, between 0 and 2.2 km s^{-1} for OH, between 0 and 22 km s^{-1} for H_2, and between 0 and 37 km s^{-1} for H. The product exothermic velocities and their corresponding velocity distributions are generally not well known because of the lack of cross sectional information as a function of wavelength for the internal energy of the molecular products [$OH(X^2\Pi)$, $OH(A^2\Sigma^+)$, and H_2] that determines the available excess kinetic energies for the products. Only upper limits are therefore given for many of the product exothermic velocities in Table 1. For different assumptions regarding the product abundances and the configuration of the internal energy of OH, examples are given in *Wu and Chen* (1993) for the velocity distributions of H and OH that bound their behaviors.

3.2. Ion and Electron Impact Water Chemistry

The solar wind plays a minor role in the destruction of water compared to photochemistry but plays an important role in the ion chemistry of the coma, which also involves many other atomic and molecular ions (*Häberli et al.,* 1997). A summary of the most relevant solar wind proton and electron reactions with H_2O and the values of the corresponding destruction rates is given in Table 2 for a nominal solar wind flux of 3×10^8 cm^{-2} s^{-1} at 1 AU as reported by *Budzien et al.* (1994). The largest water destruction rate is for charge exchange with protons, followed by electron impact ionization, proton impact ionization, proton impact dissociation, and electron impact dissociation. At 1 AU, the charge exchange rate is comparable to the photoionization rate of ~4.1×10^{-7} s^{-1} for quiet Sun conditions, but is smaller than the photoionization rate of ~1.04×10^{-6} s^{-1} for active Sun conditions (*Huebner et al.,* 1992). These destruction rates are not well established due to uncertainties in cross sections and furthermore vary significantly due to changing solar wind conditions upstream of the comet bow shock and to spatially changing properties of the ion and electron distributions in the cometosheath, outer coma, inner coma, and ion tail. The electron impact rate of 3×10^{-7} s^{-1} in Table 2 is, for example, a typical value for solar wind electrons in the outer coma, but may be considerably larger, ~1×10^{-6} s^{-1}, for electrons heated in the cometosheath, where it may be comparable to the active Sun water photoionization rate, and even larger in the inner coma where stagnation flow and photoelectrons are also present (*Cravens et al.,* 1987). The total water destruction rate for the nominal values in Table 2 is 1.08×10^{-6} s^{-1}. Since this total solar wind destruction rate varies throughout the coma, it is

TABLE 2. Solar wind destruction for H_2O vapor.

Reaction	Destruction Rate (10^{-7} s^{-1})
$H^+ + H_2O \rightarrow H + H_2O^+$	5.7
$\rightarrow H^+ + H_2O^+ + e$	0.75
$\rightarrow$ dissociated neutral products	0.27
$e + H_2O \rightarrow H_2O^+ + e + e$	~3 (variable)
$\rightarrow$ dissociated neutral products	1.1

Destruction rates for a nominal solar wind flux of 3×10^8 cm^{-2} s^{-1} from *Budzien et al.* (1994).

TABLE 3. Photochemical branching and exothermic velocities for OH.

Wavelength	OH Predissociation State	Reaction	Product Exothermic Velocities* (km s^{-1})		Photodestruction Rate (10^{-6} s^{-1}) (Quiet Sun)		(Active Sun)	
2160 Å	$A^2\Sigma^+$ (v' = 2)	OH + hν → O (^{3}P) + H	8 (H)	0.5 (O)	3.0–6.1†	2.5–5.6‡	3.0–6.1†	2.5–5.6‡
2450 Å	$A^2\Sigma^+$ (v' = 3)	OH + hν → O (^{3}P) + H	11 (H)	0.7 (O)	0.5†		0.5†	
1400–1800 Å	$1^2\Sigma$	OH + hν → O (^{3}P) + H	22–26 (H)	1.4–1.6 (O)	1.4†	1.4§	2.3†	1.58§
1216 Å	$1^2\Delta$	OH + hν → O (^{1}D) + H	26.3 (H)	1.6 (O)	0.3†	0.38§	0.75†	0.57§
1216 Å	$B^2\Sigma$	OH + hν → O (^{1}S) + H	17.1 (H)	1.1 (O)	0.05†	0.05§	0.13†	0.08§
1216 Å	$2^2\Pi$–$3^2\Pi$	OH + hν → O (^{1}D) + H	26.3 (H)	1.6 (O)	0.10†	0.24§	0.25†	0.39§
<1200 Å	$D^2\Sigma$	OH + hν → O (^{3}P) + H	22 (H)	1.4 (O)	<0.01†	—	<0.01†	—
<958 Å		OH + hν → ionized products	—	—	0.25§		0.47§	

* Product exothermic velocities from *van Dishoeck and Dalgarno* (1984) with slight updates from *Combi* (1996).
† Rates from *van Dishoeck and Dalgarno* (1984).
‡ Combined $A^2\Sigma^+$ (v' = 2 and v' = 3) rate from *Schleicher and A'Hearn* (1988).
§ Rates from *Budzien et al.* (1994).

therefore likely to alter the overall water lifetime by somewhat less than 10%.

3.3. Daughter Product Energetics and Branching Ratios in the Coma

The photochemistry and photochemical kinetics for OH have been studied in detail by a number of investigators (*Schleicher and A'Hearn,* 1982, 1988; *van Dishoeck and Dalgarno,* 1984; *Huebner et al.,* 1992; *Budzien et al.,* 1994). A summary of the relevant OH predissociation states and their corresponding dissociation reactions, product exothermic velocities, and dissociation rates, as well as OH photoionization rate, is given in Table 3 and is divided into individual contributions for various wavelengths. For the first two wavelengths at 2160 Å and 2450 Å, OH dissociates from the $A^2\Sigma^+$ state after absorption of solar radiation during the fluorescence process. The dissociation rates for these two wavelengths do not vary between quiet and active solar conditions because at these longer wavelengths the solar flux is highly stable. These two contributions to the rate, however, vary with heliocentric radial velocity, with the major contribution from the $A^2\Sigma^+$ (v' = 2) predissociation state. For the combined $A^2\Sigma^+$ (v' = 2 and v' = 3) rates, this variation is about a factor of 2 with a calculated value of 3.5–6.6 × 10^{-6} s^{-1} and of 2.5–5.6 × 10^{-6} s^{-1}, respectively, determined earlier by *van Dishoeck and Dalgarno* (1984) and more recently by *Schleicher and A'Hearn* (1988). This variation is caused because the dissociation that occurs at discrete energy levels above the dissociation threshold is produced by absorption of solar radiation, which has a solar radiation-pumping rate that varies with heliocentric radial velocity through the Swings effect (*Jackson,* 1980).

The dissociation rates for the next five wavelength entries are produced through direct photodissociation of OH in the $1^2\Sigma$, $1^2\Delta$, $B^2\Sigma$, $2^2\Pi$–$3^2\Pi$, and $D^2\Sigma$ repulsive states. These photodissociation rates, as well as that for the <958-Å wavelength entry for photoionization of OH, are listed for quiet and active Sun conditions, since the UV and extreme UV solar flux for these lower wavelengths varies significantly with solar cycle. The product exothermic velocities are distributed nonuniformly between 8 and 26.3 km s^{-1} for H and between 0.5 and 1.6 km s^{-1} for O. By adding together the second column entries in Table 3 for the newer rates and the last row entry rate, the total OH photodestruction rate then varies with heliocentric velocity from 4.82 to 7.92 × 10^{-6} s^{-1} (lifetime of 1.26–2.05 × 10^5 s) for quiet Sun conditions with more typical values of ~5.2–6.3 × 10^{-6} s^{-1} (lifetime of ~1.6–1.9 × 10^5 s) and from 5.59 to 8.69 × 10^{-6} s^{-1} (lifetime of 1.15–1.79 × 10^5 s) for active Sun conditions with more typical values of ~6.0–7.1 × 10^{-6} s^{-1} (lifetime of ~1.4–1.7 × 10^5 s). The OH photodestruction rate (lifetime) is then about a factor of 2 smaller (larger) than the photodestruction rate (lifetime) for water.

The photochemistry and photochemical kinetics for H_2, a minor dissociative species (5.1–5.5%) of water in Table 1, are summarized in Table 4, as given by *Huebner et al.* (1992). A little more than half the H_2 destruction produces two hydrogen atoms with exothermic velocities of 28 km s^{-1} and 6.3–6.5 km s^{-1}, about one-third produces H_2^+, and somewhat less than 10% produces H + H^+. The total H_2 photodestruction rate for all the reactions in Table 4 is 0.146 × 10^{-6} s^{-1} for quiet Sun conditions and 0.33 × 10^{-6} s^{-1} for active Sun conditions.

3.4. Solar Activity Variations

The primary time variability in the dissociation and ionization rates for water and its daughter products noted above arises from changes that occur in the extreme UV (λ < 1000 Å) and far UV (1000 Å < λ < 2000 Å) fluxes from the Sun. These time variations occur during the 11-year periodic solar cycle because of the variation in the number of sunspots that create enhanced extreme UV and far UV fluxes from the Sun. The distribution of sunspots on the rotating solar disk also introduces short-term 27-day modulations of the solar flux, which can be significant compared to quiet Sun conditions. The photochemistry rates sum-

TABLE 4. Photochemical data for H_2.

Reaction	Product Exothermic Velocities (km s^{-1})	Photodestruction Rate (10^{-6} s^{-1}) (Quiet Sun)	(Active Sun)
$H_2 + h\nu \rightarrow H(1s) + H(1s)$	28 (2H)	0.048	0.11
$H_2 + h\nu \rightarrow H(1s) + H(2s,2p)$	6.3–6.5 (2H)	0.034	0.082
$H_2 + h\nu \rightarrow H_2^+ + e$	—	0.054	0.11
$H_2 + h\nu \rightarrow H + H^+ + e$	—	0.0095	0.028

Product exothermic velocities and rates from *Huebner et al.* (1992).

marized in Tables 1, 3, and 4 only characterize the basic changes between the quiet and active Sun conditions and thus provide only a basic picture that may be altered significantly by short-term time variations of the solar radiation that are poorly known for observations of particular comets, except for those rare cases where the Sun-comet line crosses near one of the solar spectrum monitors [e.g., the Solar and Heliospheric Observatory (SOHO) or Solar Ultraviolet Spectral Irradiance Monitor (SUSIM)].

For convenience, the formulae are given here from *Budzien et al.* (1994) for the total water photodestruction rate $(\tau^{tot}_{H_2O})^{-1}$ and the total OH photodestruction rate $(\tau^{tot}_{OH})^{-1}$ as a function of solar activity indices $F_{10.7}$ (the 10.7-cm flux), its 81-day average, $\langle F_{10.7} \rangle$, in solar flux units 10^{-22} W m^{-2}, the solar He I λ10830 equivalent width in mÅ, the solar wind flux $\langle nv \rangle_{sw}$ in cm^{-2} s^{-1}, and the heliocentric velocity dependent predissociation rate given in tabular and graphical form by *Schleicher and A'Hearn* (1988), $[\tau^{prediss}_{OH}(\dot{r})]^{-1}$

$$(\tau^{tot}_{H_2O})^{-1} = 5.868 \times 10^{-6} + 1.49 \times 10^{-9}\, F_{10.7} + 2.08 \times 10^{-9} \langle F_{10.7} \rangle + 9.587 \times 10^{-8}\, W_{10830} + 4.1 \times 10^{-15} \langle nv \rangle_{sw} \quad (\text{in } s^{-1})$$

$$(\tau^{tot}_{OH})^{-1} = 1.479 \times 10^{-6} + 5.8 \times 10^{-10}\, F_{10.7} + 8.1 \times 10^{-10} \langle F_{10.7} \rangle + 1.678 \times 10^{-8}\, W_{10830} + 3.7 \times 10^{-15} \langle nv \rangle_i + [\tau^{prediss}_{OH}(\dot{r})]^{-1} \quad (\text{in } s^{-1})$$

4. PHYSICS-BASED MODELS

4.1. Collisional Boltzmann Equation for Rarefied Gases

The appropriate description for the physical state of any one of up to s species, p, in a multispecies dilute gas can be described by the Boltzmann equation (*Gombosi,* 1994), which is given as

$$\frac{\partial}{\partial t}(f_p) + \vec{c}_p \cdot \frac{\partial}{\partial \vec{r}}(f_p) + \vec{F} \cdot \frac{\partial}{\partial \vec{c}}(f_p) = \sum_{q=1}^{s} \int_{-\infty}^{+\infty} \int_{0}^{4\pi} (f^*_p f^*_{lq} - f_p f_{lq}) c_{rpq} \sigma_{pq} d\vec{\Omega} d\vec{c}_{lq} \quad (10)$$

where $f_p \equiv f_p(\vec{r},\vec{c},t)$ and $f_d \equiv f_d(\vec{r},\vec{c},t)$ are the full phase space velocity distribution functions for species p and q, c_q is the velocity, r is the spatial coordinate, $\vec{F}$ represents external forces, c_{rpq} is the magnitude of the relative velocity between particle p and q, Ω is the solid angle, the asterisks (*) indicate postcollision particles, the lq subscript refers to the scattering target particles, and σ_{pq} is the total collision cross section between species p and q (which can in general be velocity dependent). In the collision integral on the right-hand side of the equation, f* represents additions of particles, scattered into the region of velocity space in question, i.e., between $\vec{c}$ and $\vec{c} + d\vec{c}$, whereas f without the asterisk represents scattering out of that region.

The Boltzmann equation makes neither assumptions nor any restrictions as to the form of the distribution functions. Various velocity moment expansions of the integrals over the distribution functions yield equations of conservation of mass, momentum, and energy. The assumption of local thermodynamic equilibrium (LTE) and the resulting Maxwell-Boltzmann distribution functions yield the Euler equations for fluid dynamics. The Chapman-Enskog theory is a perturbation from the Maxwell-Boltzmann distribution, which yields the Navier-Stokes equations with viscosity and heat flux. For the intended purpose of studying tenuous atmospheres and transitions from an LTE fluid to free-flow, the basic assumptions for these approximations are inherently violated, and therefore a potentially arbitrary form for the distribution functions remains to be considered.

Direct analytical or even numerical solutions for the Boltzmann equation have been done for numbers of idealized simple problems (*Fahr and Shizgal,* 1981), for reduced spatial or velocity dimensions, or for specific analytical forms of the collision integral [see the textbook by *Gombosi* (1994) for an up-to-date treatment of gaskinetic theory]. Even one-dimensional flow problems yield three-dimensional distribution functions, one spatial and two velocity. For similar reasons the Direct Simulation Monte Carlo (DSMC) method has also been adopted to treat multidimensional, multispecies gas flows for tenuous planetary applications. In the computational fluid dynamics community, DSMC is the method of choice for validating such fluid approaches, such as solution of the Navier-Stokes equations (*Bird,* 1994). For example, the modelers of shock structures in one-dimension have typically "resorted" to Monte Carlo simulation for numerical experiments.

4.2. Time-Dependent Hydrodynamics

If one multiplies the Boltzmann equation, alternatively, by 1, v, and v^2 (where v is the gas velocity) and then integrates the resulting equations over the vector velocity, the resulting equations correspond to conservation laws of mass continuity, momentum, and energy (*Gombosi et al.,* 1986). These equations can be closed and combined with the ideal gas law to provide a useful way to understand the transport and energy of the gas in the coma. The energy and momentum equations obtained can be manipulated to yield an equation for gas pressure instead of energy. Dust-gas physics can be added in the form of dust continuity and momentum equations with standard collisional coupling terms that assume the gas mean free path is much larger than the dust size and that gas molecules accommodate to the dust surface temperature upon a collision. Since there is no random internal energy component for dust particles, no pressure/energy equation is required. For detailed derivations see the papers, for example, by *Gombosi et al.* (1986) and *Crifo et al.* (1995). The coupled system for a single-fluid gas and multicomponent dust (i.e., dust size distribution) can be written as

$$\frac{\partial \rho}{\partial t} + \nabla \cdot (\rho \mathbf{u}) = \frac{\delta \rho}{\delta t} \tag{11}$$

$$\rho \frac{\partial \mathbf{u}}{\partial t} + \rho(\mathbf{u} \cdot \nabla)\mathbf{u} + \nabla p = -\mathbf{F} \tag{12}$$

$$\frac{1}{\lambda - 1}\frac{\partial p}{\partial t} + \frac{1}{\gamma - 1}(\mathbf{u} \cdot \nabla)p + \frac{\gamma}{\gamma - 1}p(\nabla \cdot \mathbf{u}) = -Q_{gd} + Q_{ph} - Q_{IR} \tag{13}$$

$$\frac{\partial \rho_i}{\partial t} + \nabla \cdot (\rho_i \mathbf{u}_i) = \frac{\delta \rho_i}{\delta t} \qquad i = 1, \ldots, N \tag{14}$$

$$\rho_i \frac{\partial \mathbf{v}_i}{\partial t} + \rho_i(\mathbf{v}_i \cdot \nabla)\mathbf{v}_i = \mathbf{F}_i \qquad i = \ldots, N \tag{15}$$

where ρ is the gas mass density, $\mathbf{u}$ is the gas velocity, p is the gas pressure, and $\mathbf{v}_i$ and ρ_i are the velocity and mass density for dust particles of radius a_i. The righthand sides of all the equations contain the various source terms. The term

$$\frac{\delta \rho}{\delta t}$$

is the gas production source rate, and

$$\frac{\delta \rho_i}{\delta t}$$

is the dust production source rate for particles of radius, a_i. $\mathbf{F}$ is the gas-dust drag force, which is related to the forces on the individual particle size populations as

$$\mathbf{F} = -\sum_{i-1}^{N} \mathbf{F}_i$$

where the size dependent force is given by

$$\mathbf{F}_i = \frac{3\rho_i}{4a_i\rho_{bi}} p C'_D \mathbf{s}_i$$

where

$$\mathbf{s}_i = \frac{\mathbf{u} - \mathbf{v}}{\sqrt{2kT/m}}$$

k is the Boltzmann constant, T is the gas temperature and m is the gas mean molecular mass. The accommodation of gas via collisions with hotter dust yields the dust-gas heat exchange rate Q_{gd}, which is given as

$$Q_{gd} = \frac{\gamma + 1}{\gamma} \rho C_p u \sum_{i=1}^{N} (T_i^{rec} - T_i) St'_i \tag{16}$$

Here C_p is the gas heat capacity at constant pressure and the rest of the coefficients can be defined under the assumption of diffusive reflection such that

$$C'_D = \frac{2\sqrt{\pi}}{3}\sqrt{\frac{T_i}{T}} + \frac{2s_i^2 + 1}{s_i^2\sqrt{\pi}} e^{-s_i^2} + \frac{4s_i^4 + 4s_i^2 - 1}{2s_i^3} \mathrm{erf}(s_i) \tag{17}$$

$$T_i^{rec} = \left(1 + \frac{\gamma - 1}{\gamma + 1} s_i^2 R'_i\right) T \tag{18}$$

$$R'_i = \frac{\left(2s_i + \frac{1}{s_i}\right)\frac{e^{-s_i^2}}{\sqrt{\pi}} + \left(2s_i^2 + 2 - \frac{1}{s_i^2}\right)\mathrm{erf}(s_i)}{s_i \frac{e^{-s_i^2}}{\sqrt{\pi}} + \left(s_i^2 + \frac{1}{2}\right)\mathrm{erf}(s_i)} \tag{19}$$

$$St'_i = \frac{e^{-s_i^2}}{8s_i\sqrt{\pi}} + \frac{1}{8}\left(1 + \frac{1}{2s_i^2}\right)\mathrm{erf}(s_i) \tag{20}$$

Finally, ρ_d is the bulk mass density of dust particles of radius a_i, T is the gas temperature, and T_i is the dust temperature, assumed in equilibrium with solar radiation. A temperature-dependent value can be used for C_p to account for some of the effects of divergence from LTE, especially at low temperature, where all internal degrees of freedom are not available. Otherwise the other intermediate quantities are s_i, the relative Mach number between gas and dust; C'_D, the dust-gas drag coefficient; T_i^{rec}, the recovery temperature; R'_i, the heat transfer function; and St'_i, the Stanton

number. Most of the dust-gas drag physics comes from the formulation by *Finson and Probstein* (1968) with later corrections discussed by *Wallis* (1982), *Kitamura* (1986), and *Körösmezey and Gombosi* (1990).

4.3. One-Dimensional Spherical Steady-State Equations

The general three-dimensional time-dependent Euler equations of hydrodynamics can be reduced to a steady-state one-dimensional version, which is very useful for understanding the basic physical state of the outflowing coma. Again, a detailed description of the derivation was given in the review paper by *Gombosi et al.* (1986). These are

$$\rho = \frac{Qm}{4\pi u r^2} \tag{21}$$

$$\rho u \frac{du}{dr} = -\frac{dp}{dr} - F \tag{22}$$

$$\rho_i v_i \frac{dv_i}{dr} = F_i \tag{23}$$

$$\frac{1}{r^2}\frac{d}{dr}\left[\rho u r^2\left(\frac{u^2}{2} + \frac{\gamma}{\gamma - 1}\frac{p}{\rho}\right)\right] = S - L + Q_{gd} \tag{24}$$

Assuming the normal ideal gas law

$$p = \frac{\rho k T}{m}$$

the above system of equations can be solved from an initial boundary condition, e.g., at or near the surface of the nucleus. The main difficulty in implementing the steady-state version of the hydrodynamic equations is if one specifies the inner boundary at or so close to the surface of the (spherical) nucleus that the gas is subsonic, in which case the transonic transition is an undefined point. This has been addressed either using a shooting method (*Marconi and Mendis,* 1983), or by using the approach of *Gombosi et al.* (1985), which solves explicitly for the conditions at or just above the sonic point, normally only meters above the surface of a spherical nucleus with radius of typically a few kilometers. In this case F_i is purely radial and the same dust-gas drag force as used in the time-dependent equations (11)–(15).

In this case, Q in equation (21) is the simple molecular gas production rate, u is the radial gas velocity, S is the photochemical heating rate, L is the IR cooling rate. Other variables are consistent with the definitions in the previous section of this chapter. The IR cooling rate has been estimated a number of ways over the last three decades, first heuristically by *Shimizu* (1976) and then more explicitly by *Crovisier* (1984, 1989), *Crifo et al.* (1989), and *Combi* (1996). Complicating effects are that water densities are large enough in the inner coma for the IR radiation to be optically thick in some lines, and that the rotational temperature comes out of equilibrium with the gas kinetic temperature with increasing distance from the nucleus. The optical depth is normally handled with an escape probability based on the estimate of *Huebner and Keady* (1983). An approximate kinetic to rotational energy transfer rate has been incorporated into effective cooling rates by *Crovisier* (1984, 1989). The kinetic simulations by *Combi* (1996) explicitly include a microphysical description of internal rotation energy, which indicates that the earlier approximations are generally reasonable.

4.4. Hybrid Kinetic/Fluid Models

For typical comets over a wide range of gas production rates and heliocentric distances, the photochemical heating rate is not simple to calculate because the coma gas is not in local thermodynamic equilibrium. As discussed in detail in a previous section of this chapter, water photodissociation reactions provide the bulk of excess energy for the coma, with the main dissociation branch

$$H_2O + h\nu \rightarrow H + OH + \text{Energy} \tag{25}$$

providing most of the energy. Because there is excess energy after overcoming the chemical bond energy on the order of 2 eV for this reaction and the products H and OH must conserve both energy and momentum, so 17/18 of the energy is imparted to the H atom, producing it with an excess velocity of ~17.5 km s^{-1}. The OH radical, on the other hand, has an excess velocity of 1.05 km s^{-1}. Typically in modeling energy balance and transport in a planetary atmosphere, the gas densities are large enough that one can normally assume that all the photodissociative heating energy happens locally, so the heating rate is just given as the sum of the products of the local species gas density, the excess energy per dissociation, and the dissociation rate. In a comet coma the region where the gas density is large enough for local photochemical heating efficiency to be 100% depends on the overall gas production rate and the expansion velocity of the coma. In addition, because of the dominant ~$1/r^2$ fall-off of the density, the decrease of photochemical heating efficiency is gradual compared to a planetary atmosphere with an exponential scale height variation in density. It therefore is not possible to define, strictly speaking, a collision zone size for the heating caused by hot superthermal H atoms.

Ip (1983) first addressed the issue of photochemical heating efficiency for the superthermal H atoms and derived an analytical estimate. *Huebner and Keady* (1983) developed an escape probability formalism to treat the escaping superthermal H atoms, and *Marconi and Mendis* (1983) treated two populations of H atoms: a superthermal component and a thermal one to deal with the photochemical heating efficiency. *Combi* (1987) and *Bockelée-Morvan and Crovisier* (1987) performed Monte Carlo calculations for individual superthermal H atoms and modified the photo-

chemical heating rate using the accumulated collisional energy transfer. Generally the heating efficiency increases with larger gas production rates (Fig. 3) because of increased gas densities and at smaller heliocentric distance (Figs. 4 and 5) because of increased photodissociation rates. Figure 6 shows results by *Ip* (1989) for hybrid kinetic/fluid calculations of outflow speeds in Comet 1P/Halleycompared with measurements of propagating CN shells. These results are consistent with otherwise similar comparisons of different datasets by *Combi* (1989).

The complementary part of this approach is to predict the distribution of observed daughter species given a realistic physical description of the inner "parent" coma and the nonequilibrium collisional processes that alter the velocity distribution function of the daughter species. This was first done by *Kitamura et al.* (1985) for hydrogen assuming a constant velocity point source parent coma. A general time-dependent, three-dimensional approach was taken by *Combi and Smyth* (1988a,b), whereby the parent coma was described by a time-variable hybrid/kinetic calculation and applied to explain the type of empirical H-atom velocity distribution found by *Meier et al.* (1976) for observations of the shape of the Lyman-α coma of Comet Kohoutek for two very different sets of conditions. It has been successfully applied to a number of comets since then, including 1P/Halley by *Smyth et al.* (1991) and the very extreme case of C/1995 O1 (Hale-Bopp) by *Combi et al.* (2000). As shown in *Feldman et al.* (2004), in addition to being able to reproduce the spatial morphology of the coma, which is sensitive to the velocity distribution because of the large solar radiation pressure acceleration on H atoms, it was applied directly to Goddard High Resolution Spectrograph (GHRS)/Hubble Space Telescope (HST)-measured Doppler line profiles of H Lyman-α in Comet C/1996 B2 (Hyakutake) by *Combi et al.* (1998) and subsequently included in a full-wavelength-dependent radiative transfer calculation by *Richter et al.* (2000). The approach was also generalized for heavy species and applied to OH by *Combi et al.* (1993); O(^{1}D) and NH_2 by *Smyth et al.* (1995); C_2, CN, NH_2, and

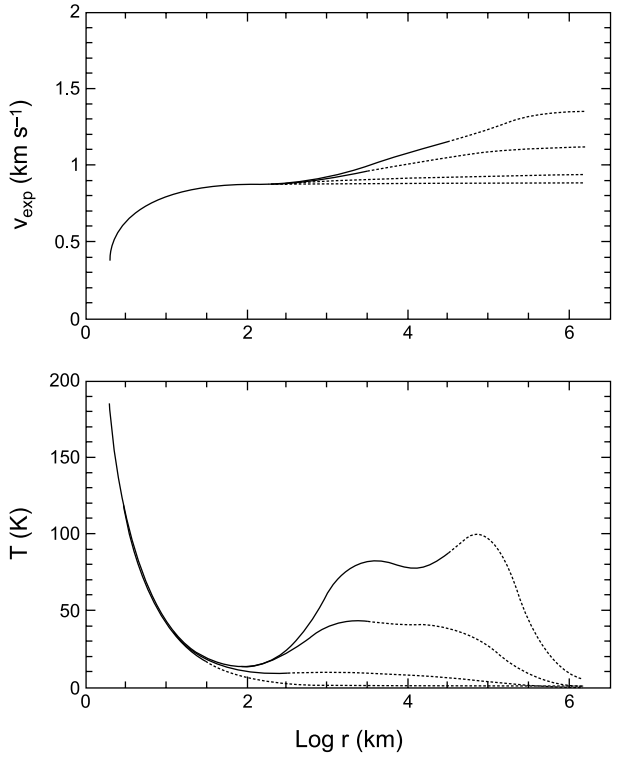

Fig. 3. The effect of coma gas production rate on radial velocity and kinetic temperature in the coma. Model calculations by *Bockelée-Morvan and Crovisier* (1987) from top to bottom for gas production rates of 10^{27}, 10^{28}, 10^{29}, and 10^{30} s^{-1}. The dashed portions of the lines correspond to the outer nonfluid region of the coma.

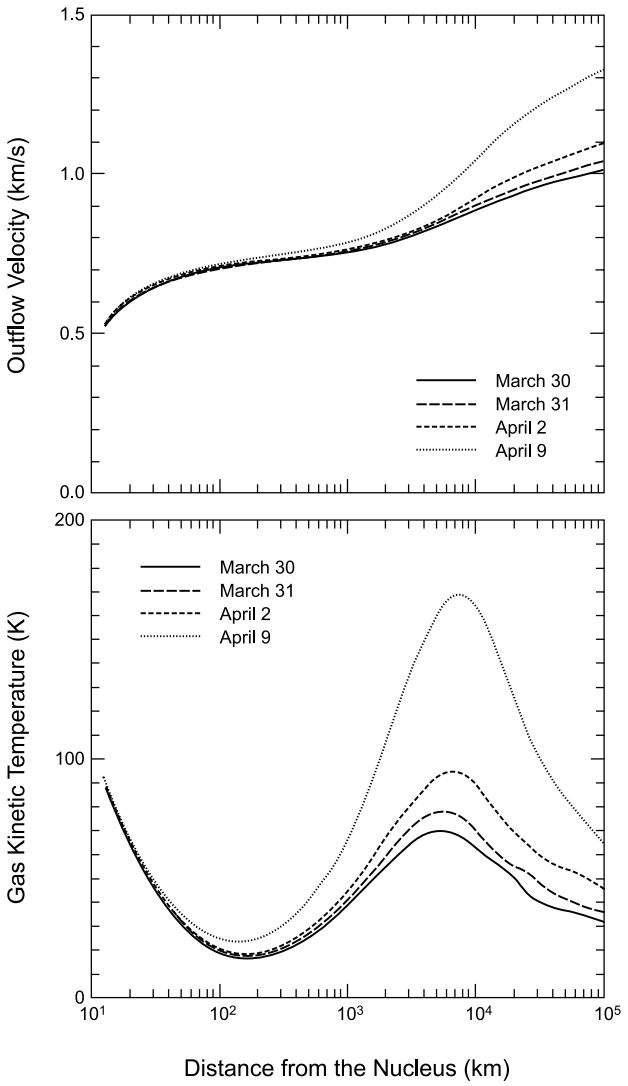

Fig. 4. Radial velocity and gas kinetic temperatures in Comet 1996 B2 (Hyakutake) from models by *Combi et al.* (1999a). Heliocentric distance varies from 0.94 to 0.71 AU. The production rates for the dates beginning with March 30 are 2.0, 2.2, 2.7, and 4.0 × 10^{29} s^{-1}.

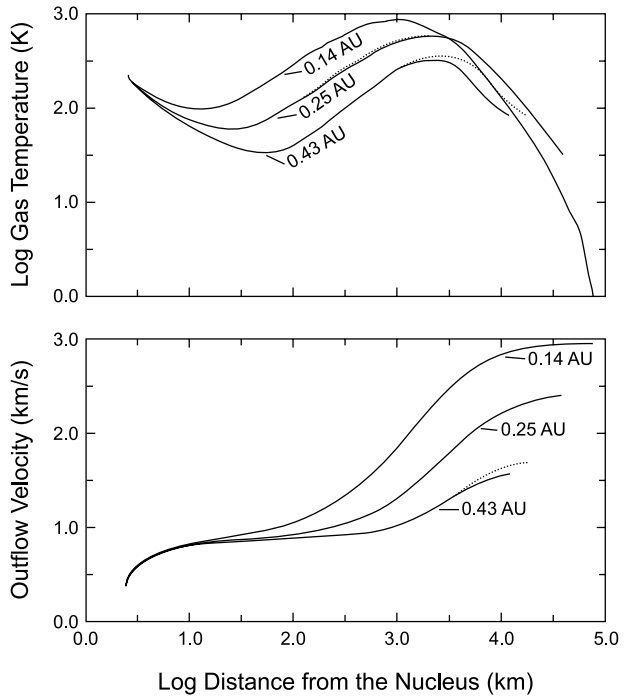

Fig. 5. Model radial velocity and gas kinetic temperatures in Comet Kohoutek by *Combi and Smyth* (1988b) for large production rate and small heliocentric distance.

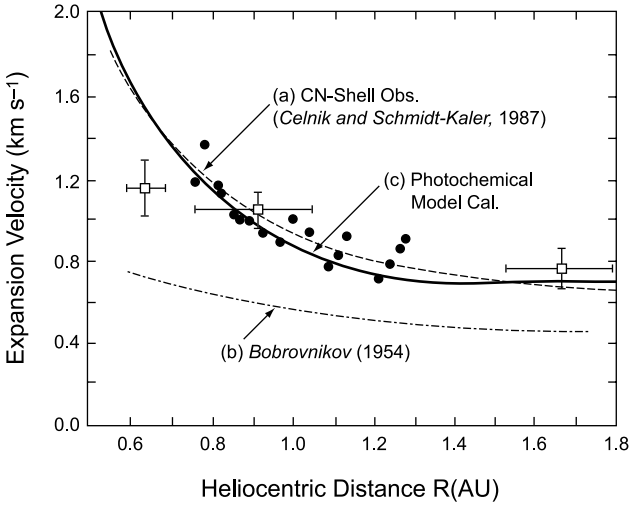

Fig. 6. Model-data comparison of expansion velocity of CN shells in Comet 1P/Halley by *Ip* (1989).

$O(^1D)$ by *Combi et al.* (1999a); and then to NH_2 by *Tegler et al.* (1992) and *Kawakita and Watanabe* (1998).

4.5. Kinetic Models

The first fully kinetic model for the water-dominated cometary coma that included a fairly complete description of the physics was presented by *Hodges* (1990). This calculation was of the test particle (TP) type. It starts with an initial assumed description for the distribution function of the gas that serves as a background for test particles of the same gases. In this particular case water molecules are emitted from the model nucleus and dissociation products (OH, H, O, etc.) are produced in a random but physically fair fashion. Collision probabilities are calculated between the test particles and current version of the background distribution functions for all species, and the test particles are scattered as necessary. A new background distribution is accumulated (or partially accumulated) from the state of the test particles in each iteration, which then serves as a new background. The premise is that once the background distribution and the test particle distribution converge to the same state, then that state describes the steady-state solution for the gas. *Xie and Mumma* (1996a,b) updated some of the statistical algorithms from the original model of Hodges, improving the sampling of velocities for collision pairs and including a more accurate description of the IR rotational cooling by water molecules.

A DSMC model proceeds by following the detailed molecular motions of many molecules (thousands to millions) simultaneously, including their responses to imposed fields (e.g., gravity, or E and B fields in the case of charged particles), binary collisions, and chemistry. The assumption of binary collisions is quite good for a dilute gas and basically requires that the gas density be such that the distance between molecules is much larger than the molecular size. Quite dense gases, for instance, the standard density at the surface of Earth, which is in the realm of hydrodynamics, easily satisfy this condition.

A DSMC model is inherently time dependent and can address a wider range of problems than TP methods. Steady-state situations are achieved by running a simulation for a long enough time given steady-state initial and boundary conditions. Therefore, the final state does not depend *per se* on the initial state provided the system is given an adequate time to relax. The initial state could start at some given state, or a vacuum. In terms of computational resources the inherently steady-state iterative TP approach requires less memory than a steady-state version of a DSMC; however, both must sample a similar number of individual particles over a similar time with similar time steps in order to model a real physical system with similar statistical accuracy. Therefore, the total number of computations between the two methods should be roughly equivalent.

A DSMC model begins by setting the initial state of a certain number of molecules of all species in question throughout the simulation volume. Various boundary conditions from which new particles are introduced into the simulation volume must be defined and characterized. The simulation is divided into small time steps, Δt_S, which must be small enough so that only a small fraction (<0.1) of particles in any volume of space will collide over that time, and so that the forces (accelerations) yield small enough velocity changes, thereby allowing some finite-difference formulation to follow the particle trajectories. Higher-order schemes can also be used for this purpose if the timescale for trajectory variations owing to outside forces (e.g., grav-

ity, or electromagnetic) is much smaller than the collision timescale. Furthermore, each spatial cell can have its own collision time step, so that useless collision testing need not be performed when the densities are quite low. This clearly occurs high enough in an atmosphere or far enough away from the nucleus in a cometary coma, and means that collisions that occur more frequently in regions of high density can be sampled as often as necessary.

There are clear advantages to kinetic DSMC methods in being able to treat a whole range of non-LTE processes as well as multiple species. At the same time there are serious computational penalties, so particle kinetic methods are not meant to be substitutes for all other modeling techniques in all applications: Clearly simple models such as Haser or vectorial and hydrodynamics approaches, such as Euler and Navier-Stokes, are highly useful.

A very useful application of DSMC to an expanding comet atmosphere was to understand the time-dependent effects of the dynamics of the expanding atmosphere of Comet 1P/Halley (*Combi,* 1996). Figure 7 shows a plot of the measured outflow speed of the heavy molecules in the coma as measured by the neutral mass spectrometer on the *Giotto* spacecraft (*Lämmerzahl et al.,* 1987) compared with time-dependent DSMC model calculations. Shown are the time variations of the dependence of the radial outflow speed on distance from the nucleus owing to the variation in the water production rate at the nucleus. The model uses a time-variable production rate at the nucleus derived from the photometric lightcurve of *Schleicher et al.* (1990) using an analysis of spatial profiles of a number of species by *Combi and Fink* (1993), which is also shown. When the production rate is large, the gas densities are high and collisional thermalization of the superthermal H atoms is efficient. This causes an increase in the photochemical heating that drives an increase in the outflow speeds. Therefore, the radial outflow speeds corresponding to peaks in the lightcurve are noticeably larger than those during the troughs. For the factor of 3–4 in production rate variation in Halley, this turned out to be a fairly sensitive change, especially when the timescale for large production rate changes is comparable to the timescale of transit of gas across the coma. As shown by the appropriate lightcurve for the phase of the *Giotto* measurements, the model predicts the measured velocities. As shown, if the comet had been at a different phase of the variation (only a day or so earlier or later), a measurably different velocity profile would have been obtained.

Skorov and collaborators have used DSMC to explore the Knudsen layer at the nucleus surface/coma boundary (*Skorov and Rickman,* 1998; *Markiewicz et al.,* 1998) and the porous upper layers of the surface of the nucleus itself (*Skorov et al.,* 2001). More recently, Crifo and collaborators (*Crifo et al.,* 2002, 2003) have been comparing calculations using DSMC and solutions of the Euler equations and Navier-Stokes equations formulation of hydrodynamics for a dusty-gas coma in the vicinity of the nucleus. They find that outside the most collisionally thick region of the coma, where the Euler equations are valid, there is a region where the Navier-Stokes equations provide a reasonable calculation of the coma density and velocity flow field, as verified in numerical experiments with DSMC. However, as mentioned above, the very near-nucleus region is discussed in *Crifo et al.* (2004). In the larger "observable" coma, which we address in this chapter, not only are the Euler equations not valid, but also DSMC is very useful to model simultaneously multiple species, including photochemical products that are far from any Maxwellian or slightly skewed Maxwellian distribution assumed for Navier Stokes. Here, DSMC is the only currently developed viable alternative.

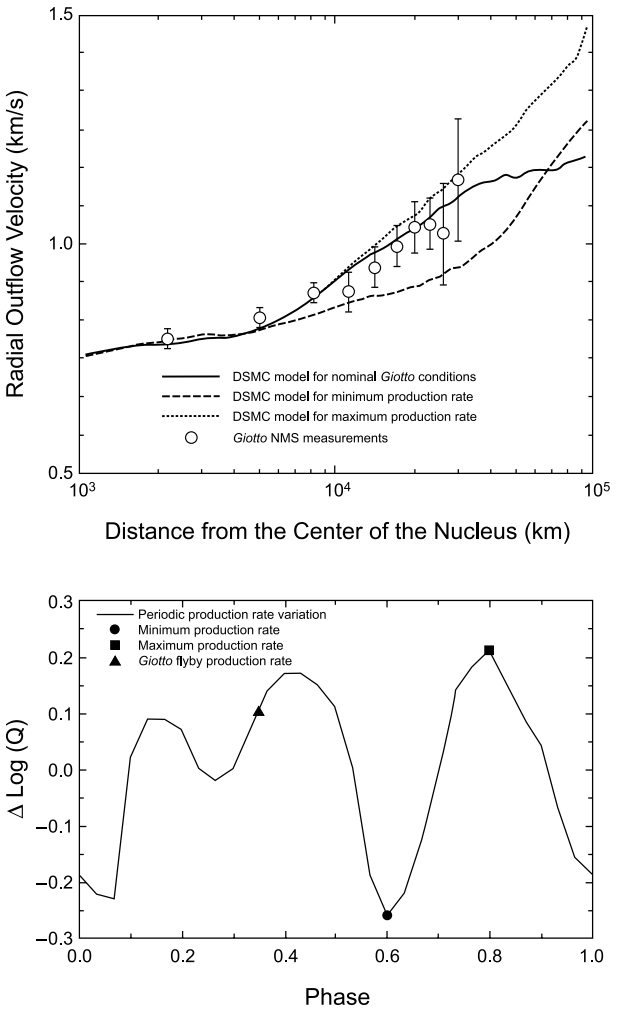

Fig. 7. Time-dependent DSMC model calculation for Comet 1P/Halley around the time of the *Giotto* encounter. In the top plot results are shown for maximum, minimum, and *Giotto* flyby phases of the lightcurve. Time variations were adopted from the photometry of *Schleicher et al.* (1990), and are shown in the plot below. The seven-day periodic gas production variation leads to 25% variations of the outflow speed.

4.6. A CO-Dominated Coma

The observed examples of CO-dominated comae are for comets at large heliocentric distances, like Comets 29P/Schwassmann-Wachmann 1 and 1995 O1 (Hale-Bopp). *Biver et al.* (1999a) found that the coma of Comet Hale-Bopp underwent a transition from CO-dominated to H_2O-dominated at a heliocentric distance of about 3 AU both before and after perihelion. There were velocity resolved millimeter-radio observations of CO, CH_3OH, and H_2CO in Hale-Bopp when the comet was at a heliocentric distance of 6 AU (*Jewitt et al.,* 1996; *Womack et al.,* 1997) and the coma was CO-dominated. The CO emission indicates primarily sunward-directed velocities of 0.3–0.4 km s^{-1} that are much larger than would be expected for an exposed sublimated CO-ice surface, which is 25 K when emitted into a vacuum (*Yamamota,* 1985). On the other hand, emissions from CH_3OH and H_2CO indicate a more isotropic ejection that possibly points to an extended source by photodissociation of parent molecules and/or sublimation from icy grains. The most reasonable explanation is that CO is likely released from the dayside of the nucleus when the subsurface thermal wave causes the dominant H_2O ice to undergo a phase transition from crystalline to amorphous ice, which happens at about 125 K (*Prialnik et al.,* 2004). At such a temperature, CO would be released from the ice below the surface and could diffuse through porous upper layers of the nucleus surface. A temperature of 125 K is consistent with the observed velocity.

There has been little theoretical work done on the possible conditions in the coma of a comet that is dominated by CO. *Ip* (1983) computed a photochemical/hydrodynamic model for a CO-dominated comet at a heliocentric distance of 1 AU, conditions which, we know now in hindsight, are unlikely to occur. Observations of comets to date would indicate that any comet at a heliocentric distance of 1 AU would be water-dominated. The model assumes that the gas is released from the surface at the vapor-pressure-equilibrium sublimation temperature of CO ice, which is 40 K. The photochemical heating effects of CO at 6 AU are negligible compared with the model at 1 AU because of the increase of the CO lifetime by a factor of 36, and this is compounded by a production rate for Hale-Bopp that was only a few $\times$ 10^{28} molecules s^{-1}, and the fact that CO is a reasonably efficient at cooling in the IR (*Chin and Weaver,* 1984). This would result in any energetic photodissociation products (hot superthermal C and O atoms) to be emitted well outside the collision zone for this comet.

More recently, *Crifo et al.* (1999) presented results of aspherical models for CO-dominated comae of Comets 29P/Schwassmann-Wachmann 1 and 46P/Wirtanen. They assumed that CO diffuses through the surface of a comet at a heliocentric distance of 3 AU, which reaches the local equilibrium temperature of a blackbody with values ranging from 230 K at the subsolar point to 41–73 K on the nightside depending on the value of a surface recondensation parameter. Such large temperatures lead to large outflow velocities at a few nucleus-radii in the range of 0.65–0.75 km s^{-1} or more. Accounting for the expected temperature differences between 3 and 6 AU does not explain the factor-of-2 smaller observed speed in Hale-Bopp. So, at least for the case of Hale-Bopp, their surface temperature model is too hot, but the basic physics of the flow velocity is otherwise reasonable. Clearly, the CO reservoir temperature from Hale-Bopp was less than the expected surface temperature. This either says something important about the surface temperature for these comets at 6 AU or more likely about the temperature accommodation for CO gas effusing through the upper porous layers.

5. SPATIAL AND VELOCITY MEASUREMENTS: OBSERVATIONAL TECHNIQUES AND MODELS

The methods used to study the composition and structure of comet comae are beginning to reach the point where gas production rates, energy balance, chemistry, velocity structures, radial distributions, temporal-spatial variability, and the interaction of the coma with solar wind are all accessible at some level with remote sensing, although the inversion of data to physical parameters continues to require model interpretation and coordinated complementary observations. Maturation of these techniques has been both technical and physical. The widespread use of linear, high-dynamic-range detectors has improved sensitivity and photometric accuracy in the visible, while advances in digital quantum efficiency and array size have combined with larger telescope apertures to increase the absolute sensitivity limit and angular scale over which comets are studied. Substantial improvements in UV, IR, and radio instrument capabilities have made accessible many minor species, thermal diagnostic bands, and faint or previously undetectable emissions from parent species and their atomic end states, while new developments in interferometric, high-resolution, and integral-field (multipoint) spectroscopic techniques have opened up the study of fine structure and the low-velocity (<1 km/s) characteristics in different regions of the coma. Finally, our ability to monitor the variable elements of the solar UV spectrum that drive photochemistry has improved our ability to validate theoretical rate calculations and to separate the linked variables of velocity and lifetime in expansion models.

To take full advantage of these improved observational capabilities requires corresponding improvements in our understanding of how photolysis, branching ratios, and fluorescence efficiencies of a chemical species affect its role and evolution in the coma, and of how the detailed structure of the coma affects the convergence of measurement, models, and their relationship to actual conditions. In this section we describe the most widely used techniques for remote sensing of the evolution of the H_2O coma, with an emphasis on spatial distributions, photometric measure-

ments, and spectroscopic study of line shapes and Doppler shifts [see *Feldman et al.* (2004) for an expanded discussion of spectroscopy]. We emphasize observation and modeling of the evolution of water and its daughters in the applied examples; however, it should be clear how these techniques and their limitations are applicable to other coma species. Each of these techniques is specialized to the desired feature (radial distribution, velocity profile, total production rate) or spatial scale (inner vs. outer coma) under study, or is either instrumentally [e.g., Far Ultraviolet Spectroscopic Explorer (FUSE)] or physically (e.g., quenched radio or metastable emissions) limited to specific regions of the coma. Such focus means that a detailed understanding is rarely achieved with an isolated observation, and we discuss the value and challenges of a synergistic, coordinated observational approach for modeling the full dynamic and photochemical evolution of the coma.

5.1. Remote Sensing of the Spatial, Thermal, and Velocity Properties of Cometary Water

The observational strategies used to study the H_2O coma spatially, photometrically, and in velocity space can be broken down into five areas: (1) aperture summation (wide and narrow field); (2) one- and two-dimensional mapping (narrow bandpass imaging, spectro-imaging, multiplexed spectroscopy); (3) velocity-resolved imaging (interferometric data cube studies); (4) aperture-summed line-shape measurements (high-resolution/étendue spectroscopy); and (5) temperature sensing. Each of these techniques provide a distinct diagnostic of a given species such as total production rate, spatial distribution, temporal variance, temperature, or velocity distribution, all on spatial scales ranging from the extreme inner coma (10^2–10^3 km) to the diffuse outer coma and ion tail (10^5–10^7 km). The results necessarily reflect the target diagnostic of the observation in the coma/tail region where the information is sought, which limits the scope of a model interpretation.

5.1.1. Aperture summation. Being essentially the case of zero-dimensional imaging, aperture summation is used to detect faint or low surface brightness features, multiple lines of a single molecular band, and/or to provide the highest possible photometric accuracy on a single coma component. The measurements are done either with a combination of narrow bandpass target-continuum filter image subtraction (*Schleicher et al.,* 1998; *Kiselev and Velichko,* 1999; *Grün et al.,* 2001) or spectrophotometrically (*Schultz et al.,* 1993; *Oliversen et al.,* 2002). In addition to providing high photometric accuracy, aperture summation is a useful tool for obtaining production rates. This is particularly powerful for the case of wide-field measurements that sample the entire scale length of a given species. For fluorescence, such measurements invert directly to production rate requiring only knowledge of the transition g-factor and lifetime via

$$Q_x = 10^6 I_x \Omega \Delta^2 / (g_x \tau_x) \quad (26)$$

where Ω is the solid angle of the field of view (FOV) in radians; Δ is the geocentric distance (cm); τ_x is the photochemical lifetime of species X in seconds; I_x is the field-averaged brightness in Rayleighs; and g_x is the fluorescence efficiency (photons s^{-1}). In a model inversion of resonance line photometric data we are limited by the precision of our knowledge of lifetime and fluorescence efficiency. In the case of metastable prompt emissions, a single photon is produced, which simplifies the relationship such that the production rate follows directly from the brightness (*Schultz et al.,* 1993)

$$Q_x = 4\pi\Delta^2 \Omega I_x \quad (27)$$

with the parent production rate following from the chemical branching ratio to the metastable species. The accuracy of metastable photometry is similarly limited, in this case by our knowledge of the formation rate from its parent(s) and the contribution of loss/production mechanisms that are important in the inner coma. Neither relationship accounts for potential complications such as collisional or chemical quenching, opacity to solar photolyzing or scattering radiation, or Swings/Greenstein g-factor variation (irrelevant for metastable emissions), all of which introduce uncertainties that must be addressed in the model interpretation. Even when these ancillary factors are correctly addressed, the resulting photometric measurement will represent a time-averaged production rate for the period of travel across the aperture for the slowest-velocity component of the target species.

To derive production rates when the FOV is less than the diameter of the scale length, the above relationships must be adjusted by an aperture correction (AC) term that accounts for emission beyond the edge of the aperture. The value of AC is determinable using model estimates of the scale lengths ($\gamma_x \sim v_x \tau_x$) of the species under study and its parent using either simple spherical expansion (Haser-type) or streaming particle (vectorial or Monte Carlo) models, or observationally by comparing the models to the total signal obtained by moving apertures (*Oliversen et al.,* 2002) to different locations in the coma or using apertures of different angular sizes. Coarse scale-length estimates are relatively straightforward for species (e.g., OH) in simple radial outflow assuming a static, symmetric quasithermal velocity relationship such as the $v_r \sim 0.85\, R_H^{-0.5}$ (where v_r and R_H are the outflow velocity and heliocentric distance) of *Budzien et al.* (1994). However, a precise scale-length measurement is far more complicated if there are substantial nonthermal components, e.g., for H (*Richter et al.,* 2000), if there is significant acceleration across the coma (*Harris et al.,* 2002; *Combi et al.,* 1999b; *Bockelée-Morvan et al.,* 1990), temporal variability in gas production, or an extended source region. At the low end of aperture size, where only the inner coma is sampled [e.g., FUSE (*Feldman et al.,* 2002) or the CSHELL spectrometer on the IRTF (*Dello Russo et al.,* 2000)], the above complications become more significant, while other unresolvable factors, including quenching, collisional chemistry (*Komitov,* 1989), accelerations, and/or asymmetries (spatial *and* temporal) in gas pro-

duction further confuse the interpretation. For observations of parent species with apertures that are small compared with the molecular scale length, one can use the relation that is identical to equation (2) where the number of molecules can be extracted knowing only the outflow velocity.

5.1.2. One- and two-dimensional spatial imaging. Spatial maps of the coma are obtained using interferometric imaging in the radio, spectroscopic imaging in the visible, fiberoptically multiplexed or image-sliced spectral techniques, long-slit imaging spectroscopy (low to high resolution), and narrow bandpass filter images targeting specific neutral species, ions, and dust continuum points (see *Schleicher and Farnham,* 2004). After the removal of sky, continuum, and detector background the resulting data provides a snapshot of the radial, azimuthal, and temporal structure of a coma species. Spatial data cube spectroimages of different lines in thermally diagnostic molecular rotational bands can also be used to track the evolving thermal properties of the coma. Such two-dimensional measurements are of immense value for model analysis as they contain records of gas production variability, extended source distributions, radial column density profiles, scale-length information, and local temperature, although they do come at the expense of photometric accuracy in the lower surface brightness outer coma.

Long-slit spectra provide single-dimensional spatial maps of brightness with radial distance from the nucleus. These spectra are most useful for measuring radial profiles of several species at low spectral resolution and providing velocity dispersion, Doppler shifts, and line ratios in a single molecule at medium/high resolution. As with two-dimensional imaging, slit spectroscopy is less effective in the outer coma where the surface brightness of the emissions is low. To extract radial information from the faint, diffuse outer coma, a spatial summing technique can be applied to a two-dimensional image that collapses the azimuthal dimension of a spectrally filtered image into a single averaged profile of brightness as a function of distance from the nucleus (i.e., a ring sum). Azimuthally averaged data provides much greater sensitivity to the radial profile in the outer coma, where the shape is strongly dependent on the outflow velocity distribution. However, averaging blurs spatial and temporal structure in azimuthal averages and leaves the resulting profile underconstrained, which can make it difficult to obtain a unique or consistent model interpretation. Ideally, a hybrid approach to spectroimaging data is applied, where spatial information on the underlying structures of the coma, including diurnal variances, temporal changes in overall production, vectored flows, jets, temperature, and secondary sources, are retained in the high surface brightness regions of the coma, while the more diffuse regions are summed to increase signal to noise. This greatly increases the amount of information available for model analysis, resulting in a more detailed picture of coma structure.

Inversion of a one-dimensional or two-dimensional spatial dataset to production rate can be achieved in two ways, either by summing all the photons in the FOV as an effective aperture and using equations (26) and (27), or by modeling the radial shape with spherical expansion or streaming particle models that require some additional knowledge of the outflow velocity distribution and/or chemical lifetime. In the case where the detectable dynamic range of the image extends from the inner coma to the edge of the target species scale length, a photometrically derived production rate can be combined with radial data to put constraints on the production rate and velocity distribution (*Harris et al.,* 2002) and hence constrain the uniqueness of the model fit. However, if the usable (above detection threshold) FOV is less than the scale length of the species under study, a combination of photometry and model is required. Since spatial mapping does not provide velocity information (fiber-optically multiplexed and image sliced spectral maps are an exception), the same limitations on velocity estimates hold for imaging studies that are encountered in aperture photometry and the accuracy of the production rate will depend on the precision of the estimate.

5.1.3. Velocity-resolved aperture photometry. An accurate measurement of the velocity distribution for a coma species is critical to a detailed understanding of its spatial distribution, chemistry, temperature, and evolution, particularly when using detailed models that are capable of addressing multiple component, accelerating, and/or nonradial line profiles (e.g., DSMC or hydrodynamic models). Medium resolution enables the detection of Doppler-broadened or -shifted components of emission lines (e.g., *Larson et al.,* 1987), but it is generally not sufficient for resolving the expansion velocities (1–10 km/s) of most coma species. The very high spectral resolution ($R \gg 10^5$) needed to detect low-velocity flows is problematic for narrow-aperture grating-type spectrographs, because the required combination of high signal to noise and high spectral resolution is difficult to achieve for the low surface brightness emissions that describe the coma and ion tail beyond the immediate vicinity of the nucleus. Aperture-summation techniques provide far greater étendue and thus sensitivity to diffuse emissions such as those in comet comae, and radio frequency measurements of OH and other molecular radicals (e.g., CO, HCN, H_2O) have emerged as an effective technique for detection of outflow velocity signatures as small as 0.1–1 km/s (*Bockelée Morvan et al.,* 1990; *Biver et al.,* 1999a; *Colom et al.,* 1999). Fabry-Pérot and spatial heterodyne spectroscopic (SHS) interferometers have been used to study expansions from atomic species, primarily H (*Morgenthaler et al.,* 2002) and O(^{1}D) (*Smyth et al.,* 1995) at velocity resolutions of up to 1 km/s. H Lyman-α absorption cells (*Bertaux et al.,* 1984) have also proven effective for measuring the velocity structure of coma hydrogen at subkilometer-per-second resolutions, albeit with substantial temporal averaging as the comet velocity must change with respect to the instrument to sample the full line shape. These observations all share the common limitation that they average velocities over large areas of the coma.

As a precision photometric technique, velocity-resolved aperture summation is directly invertible to production rate, subject to the same caveats described above. Because these measurements average all the velocity structures that are

detectable in the aperture, acceleration in active comets (*Colom et al.,* 1999) or changes in the velocity distribution due to radial-distance dependent photochemistry (i.e., H) (*Richter et al.,* 2000; *Combi et al.,* 1998; *Morgenthaler et al.,* 2002) are mixed both azimuthally and radially in the measured line profile and can only be partially separated with model analysis. An additional complication arises in the form of quenching in the inner coma that can render the velocity structure inner coma undetectable for some water daughter species, including OH (*Schloerb,* 1988) and O(^{1}D) (*Festou and Feldman,* 1981; *Smyth et al.,* 1995; *Morgenthaler et al.,* 2001). While the effect of quenching on the inversion to production rate can be compensated for with correction factors, the measured velocities are isolated to the regions beyond the quenching radius. This is not a problem for weak comets where the aperture is much larger than the quenching radius and the OH velocity is largely invariant, but can be severe for very active comets such as Hale-Bopp where substantial acceleration occurs in the quenched regions (*Colom et al.,* 1999, *Harris et al.,* 2002).

5.1.4. Velocity-resolved spectroimaging. Spatially discrete velocity data can be obtained from velocity-resolved interferometric (data cube) imaging, one dimensional spatial SHS, or long-slit or spatially multiplexed echelle spectroscopy. Long-slit [e.g., *Combi et al.* (1999a) at R = 200,000] and SHS [e.g., *Harlander et al.* (2002) at R = 40,000] techniques are both limited to a single dimension, but have demonstrated the very high intrinsic resolution necessary to resolve the low expansion velocity coma neutrals. Of the two, SHS offers much higher intrinsic étendue, can be tuned to very high ($R \gg 10^5$) resolution, and is better suited for observations of the outer coma or very diffuse emissions, due to the fact that the instrument collapses the dimension orthogonal to the spatial direction into the interferogram. This single-dimensional summing improves s/n as with aperture summation, but spatially averaging only one dimension, leaving radial data in the other. Echelle spectra sample smaller regions and thus probe the velocity structure at discrete locations where the surface brightness of the emission is high. This offers a more constrained measurement for model analysis, but at the expense of s/n. Echelles are more easily tuned than SHS instruments, and they have much greater flexibility in the selection of bandpass, often covering broad ranges of wavelength.

Data cube images are typically obtained interferometrically (such as a Fabry-Pérot) using a tunable filter bandpass and stepped in wavelength across a target emission feature or features (*Morgenthaler et al.,* 2001). The resulting image arrays have the velocity or line ratio distribution for every spatial element (radial and azimuthal) in the FOV and are very useful for identifying vectored flows, temperature variations, acceleration, and signatures of secondary or extended sources. Their limitation comes from the fact that they collapse the full free spectral range of the interferometer into image space, and they are generally much lower in spectral resolution ($R \leq 10^4$) in this mode than if the same instrument is used as a line-resolved aperture photometer. This makes it useful only for species with substantial nonthermal velocity components (e.g., H_2O^+ or H) or where multiple, spectrally separated lines must be ratioed (e.g., for temperature or equilibrium-state measurements).

Multiplexed spectroscopy is a powerful, hybrid technique that combines the spectral range, resolution, and étendue limitation of an echelle spectrograph with the two-dimensional coverage of an interferometric image. Tunable multiplexing spectrometers place multiple (~100) feeds at different locations over the FOV (*Anderson,* 1999), providing maps of velocity at discrete points over a wide area of the coma. Fixed multiplex arrays consist of multiple feeds covering a single FOV. In each case, the separate feeds are directed to points along a long-slit axis of an imaging echelle spectrograph. The inputs tend to be small (approximately few arcseconds in diameter) and cannot be co-added easily. This limits their sensitivity to low surface brightness emissions in the coma. Their resolution depends on the configuration of the bench spectrograph used ($10^3 < R < 10^4$).

5.1.5. Thermal measurements in the coma. A measured temperature in the coma depends on the species observed, its formation pathway, and the collision rate both in the inner coma and at the location where the measurement is taken. Such measurements thus provide an important constraint on gas-kinetic models and a link from them to the physical properties of the nucleus and surrounding volatile-rich material. Remote sensing measurements are able to provide kinetic temperatures for a number of coma species, including the primary parent species CO (e.g., *DiSanti et al.,* 2001; *Biver et al.,* 2002; *Feldman et al.,* 2002; *Brooke et al.,* 2003) and H_2O (e.g., *Mumma et al.,* 1986; *Crovisier et al.,* 1997). Owing to the absence of molecular bands for these species in the visible, the bulk of thermal remote sensing is done in the IR and at radio frequencies, although *Feldman et al.* (2002) have recently demonstrated that the kinetic temperature of CO can be obtained with FUSE observations of the 0–0 band at 1080 Å.

Mumma et al. (1986) first reported on measurements of the spin temperature of water in the coma of 1P/Halley, obtaining a value of ~40 K from the ortho-para (O-P) ratio of lines, which are assumed to be fixed at the long-term average solid-state temperature before evaporation, in the ν_3 band at 2.65 μm. Similar measurements of the H_2O kinetic temperature have been performed since, using the same and different bands (e.g., *Crovisier et al.,* 1997) as well as for O-P ratio of different coma species [e.g., NH_3 (*Kawakita et al.,* 2001)] with comparable results.

Rotational diagram derivations similar to those made in the interstellar medium have also been used to derive kinetic temperatures in comets by looking at the ratios of different rovibrational lines in a diagnostic band. These derivations produce results similar to the O-P measurements where they have been compared directly [e.g., H_2O from 1P/Halley by *Bockelée-Morvan* (1987)] and have proven effective for obtaining temperatures from several species including CH_3OH (*Bockelée-Morvan et al.,* 1994), H_2S (*Biver et al.,* 2002), and CO (*Biver et al.,* 2002; *Feldman et al.,* 2002). In par-

ticular, *Biver et al.* (2002) reported a combined study of all three of these as a function of heliocentric distance for Comet C/1995 O1 (Hale-Bopp). In addition to demonstrating consistent thermal properties between these species, they show results extending from 1 to 8 AU. While Hale-Bopp was an extreme high case for comet activity, their results demonstrate that temperature measurements are possible for many comets over the full range of their activity cycle, which will enable more detailed study of the gas kinetic evolution of the coma.

5.2. Measurements of Water and its Photochemical Products

Water itself has no visible band signature and is difficult to observe in general. Even as new techniques evolved that enable direct mapping of the water coma in the IR (*Mumma et al.,* 1986; *Crovisier et al.,* 1997; *Dello Russo et al.,* 2000) and radio (*Lecacheaux et al.,* 2003), the most common method of study continues to be observing the evolution of the daughter and granddaughter species of its photochemistry. The primary channels of this are given in Tables 1 and 2 above, with the distributions of H, H_2, metastable O(^{1}D), OH, and H_2O^+ being the major products of interest. Each species provides different elements of the water evolution picture that depend on the observational and modeling methods (described above) that are used to examine them. Here we describe most common observational approaches to each water daughter and discuss where they are useful for characterizing the coma with respect to various model approaches.

5.2.1. OH diagnostics. OH is the most commonly studied of the water daughters, with ground-detectable signatures in the NUV [the 0–0 band is the highest contrast emission feature on groundbased spectra; see Fig. 1 in *Feldman et al.* (2004)], radio (18 cm), and IR (*Crovisier et al.,* 1997) that contain complementary information about its production rate, velocity structure, and spatial distribution in the coma. OH is formed almost exclusively from water dissociation, which makes it the most easily inverted back to a parent (water) production rate. Indeed, given the single formation path of OH and the relative difficulty of observing water directly (see *Bockelée-Morvan et al.,* 2004), OH has generally been the most effective proxy for water production with the least ambiguity in its interpretation, especially for comets that are not productive and in the range of 1 AU (or less) from the Sun. For this reason the large database of International Ultraviolet Explorer (IUE) and HST observations (see *Feldman et al.,* 2004) is particularly useful for a hard calibration for the water production rate in comets.

The complexities of OH photochemistry and interpretation are described in more detail above and in *Feldman et al.* (2004); however, to summarize, the primary issues are a lack of knowledge of basic characteristics and observational difficulties. OH is difficult to isolate in a laboratory setting (e.g., *Nee and Lee,* 1985), which requires a somewhat circular study of this species where the properties of the molecule must be derived or verified by using a comet as an astrophysical laboratory. In addition, the primary observing factors that complicate the use of its NUV emission features as a diagnostic include variable atmospheric attenuation of ~2.2 magnitudes/airmass (*Farnham et al.,* 2000) when observed from the ground, and a complex Swings-Greenstein sensitivity in the g-factors of individual lines of the unresolved 0–0 band (*Schleicher and A'Hearn,* 1988). The 18-cm OH radio emissions are strongly quenched (*Schloerb,* 1988), which restricts the sensitivity of the measurement to the outer coma, an effect that becomes acute for active comets such as Hale-Bopp where the quenching region exceeded 10^5 km (*Schloerb et al.,* 1999; *Colom et al.,* 1999). Finally, there is strong photochemical sensitivity to variable UV emissions in the solar spectrum in its production and loss rates and its excitation from OH. Considerable effort has been expended toward addressing all these complicating factors, which has greatly improved the convergence between the different techniques used to study this species.

OH is observed using a combination of aperture photometry, both for radio and NUV emissions, velocity-resolved measurements (Fig. 8) in the radio (*Colom et al.,* 1999; *Bockelée-Morvan et al.,* 1990; *Crovisier et al.,* 2002), and spatial maps in the NUV (*Harris et al.,* 1997, 2002). OH has been also observed in the IR by way of fluorescent and prompt emissions in the 3-μm region (*Brooke et al.,* 1996; *Crovisier et al.,* 1997; *Mumma et al.,* 2001). Both the 0–0 band and the 1–0 band at 2850 Å are also observed from spacebased platforms (*Weaver et al.,* 1999). However, sys-

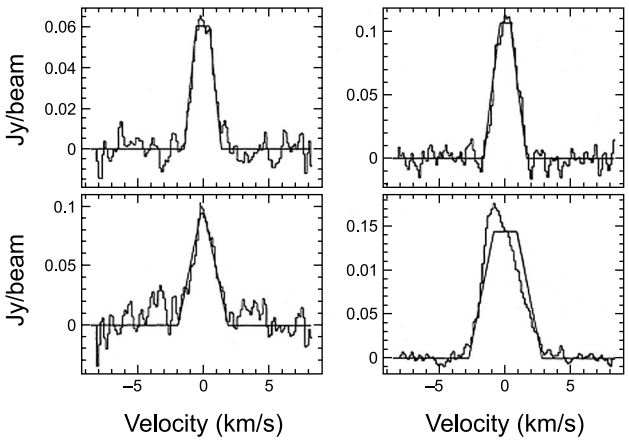

Fig. 8. OH emission at 18 cm from Comet 1P/Halley obtained with the Nançay radio telescope (3.5 × 19 arcmin beam) and using aperture summation is fit using the trapezoid method to determine the outflow velocity of the coma (from *Bockelée-Morvan et al.,* 1990). In the lower left image, the sharp peak of the fitted line is indicative of a case where $v_{parent} \sim v_{ejection} \sim 1000$ m s^{-1}. The upper two profiles are matched with flat-topped fits consistent with expansion of ~500 m/s, while in the lower right a higher, asymmetric expansion rate is obtained.

tematic spacebased observations of OH ended with the deactivation of the IUE in 1996. Following the work of *Scheicher and A'Hearn* (1988) it has been possible to correct for g-factor and scale-length variability for the NUV fluorescent bands. The inversions of photometric and spectrophotometric measurements of OH to obtain water production rates with the use of spherical expansion models for the radial distribution (*Schleicher et al.,* 1998; *Kupperman,* 1999; *Harris et al.,* 2002) are generally consistent with other estimates of water production. *Schloerb* (1988) has developed a formulism for addressing quenching of radio emissions that is comparably robust, while *Bockelée-Morvan et al.* (1990) have developed a line-fitting technique (the "trapezoid method"; Fig. 8) for determining the average radial outflow velocity in radio-band OH emissions from beyond the edge of the quenching region. This also puts some constraints on the OH ejection velocity, which is sometimes slightly discrepant with that expected from photochemical analysis (Table 1). However, these might be explained by uncertainties in the photochemical data as well as simplifications in the models, which treat the coma as spherically symmetric, collisionless flow and having a constant uniform outflow velocity for parent species.

The major limiting factor with remote sensing of OH is the relatively large number of independent unknowns that must be relied upon to model an isolated observation, with each technique requiring different approximations (azimuthal-temporal averaging, reduced outer or inner coma sensitivity, lack of velocity data, etc.). As a result it is difficult to reconcile model results from different measurements to within the relative precision of the measurements (*Schleicher et al.,* 1998). This nonconvergence is most effectively dealt with through the use of coordinated measurements (see below) that act to constrain the individual uncertainties of each observation, such as a lack of velocity data in NUV images/photometry and a lack of spatial information and the inner coma distribution in radio observations (*Harris et al.,* 2002; *Colom et al.,* 1999). Future technical developments in high étendue/spectral resolution measurements of diffuse emissions in the outer coma (*Harlander et al.,* 2002) and long-slit echelle spectroscopy of the individual lines of the 0–0 band (*Combi et al.,* 1999a) will improve the accuracy of the interpretation. It should be noted, however, that the divergence of techniques is small relative to other species, and that Q_{OH} rarely varies by more than 50% between them unless there is considerable undetected (by one measurement relative to another, e.g., narrow vs. wide field) spatial and/or temporal variation in gas production, or a difference in the underlying assumptions (e.g., outflow velocity or g-factor) used.

5.2.2. Hydrogen diagnostics. Hydrogen arguably provides the greatest physical information on the chemistry of water, the structure of the coma, and temporal variability in gas production; however, its long scale length necessitates multiple observations on different spatial scales to fully characterize its evolution. Atomic H is derived largely from water and OH dissociation, which makes it possible to derive a production rate directly, assuming the branching ratios to the multiple formation pathways are known for the conditions of the observation. The H coma is the most extended structure in comets, with observable emissions out to more than 10^7 km from the nucleus (*Combi et al.,* 2000).

Compared to the other water daughters, the H velocity distribution is completely dominated by its nonthermal elements, with H_2O and OH photochemistry contributing from 4 to 24 km/s in excess velocity. The bulk velocity distribution of H is also affected by collisions, which partially thermalize the energetic neutral H population in the inner coma, especially in very active comets (*Morgenthaler et al.,* 2001). In addition, radiation pressure modifies the distribution with an antisunward acceleration that becomes significant in the outer coma. The net result is that the velocity distribution is highly dependent on the region of the coma being sampled, the optical depth of the inner coma to solar UV radiation (both for photochemistry and resonance scattering), the total gas production rate, any short-term gas production rate variability, and the comet heliocentric velocity (for both Swings and Greenstein effects). Modeling of the distribution from the inner coma of several comets (*Combi and Smyth,* 1988a,b; *Smyth et al.,* 1991; *Combi et al.,* 1998; *Richter et al.,* 2000) nominally verifies the theoretical estimates of the velocity and its variation with heliocentric and cometocentric distances for a variety of activity level comets.

The observational challenges to the study of H in comets include the requirement for observations above the atmosphere to detect H Lyman-α or H Lyman-β, the need for measurements over multiple FOV, and strong telluric and galactic backgrounds at Hα. The primary diagnostics are resonantly scattered H Lyman-α at 1216 Å and cascade Hα emission at 6562 Å. Detection of both dates back to the C/1973 E1 (Kohoutek) apparition, with a dataset that includes most active comets since then (*Huppler et al.,* 1975; *Keller et al.,* 1975; *Drake et al.,* 1976; *Scherb,* 1981). In recent years and until the introduction of the SOHO/SWAN instrument, H observations of comets were mainly accomplished using variable width and line-resolved aperture photometry with interference techniques on medium to large spatial scale (*Morgenthaler et al.,* 2002) or echelle spectroscopy near the nucleus (*Richter et al.,* 2000; *Feldman et al.,* 2004). SOHO/SWAN has added the ability to image the full H coma (Fig. 9) and even the shadow cast by the coma on the background interplanetary medium. Because of the high energies and velocities involved in the formation of H, the contributions from the various dissociation pathways can be seen in the H Lyman-α line shape with intermediate ($R > 10^4$) resolution instruments, which increases the range of techniques and available instrumentation for the study of this feature.

H line-profiles can be compared with detailed models, albeit typically as azimuthal and radial averages over the instrument FOV, to determine the contributions from different dissociation pathways both as a function of location in the coma and as a function of overall gas production. Figure 9 compares the model simulations of the velocity distribution for Comet Hale-Bopp (*Combi et al.,* 2000) when the comet was at its most active near perihelion (0.9 AU),

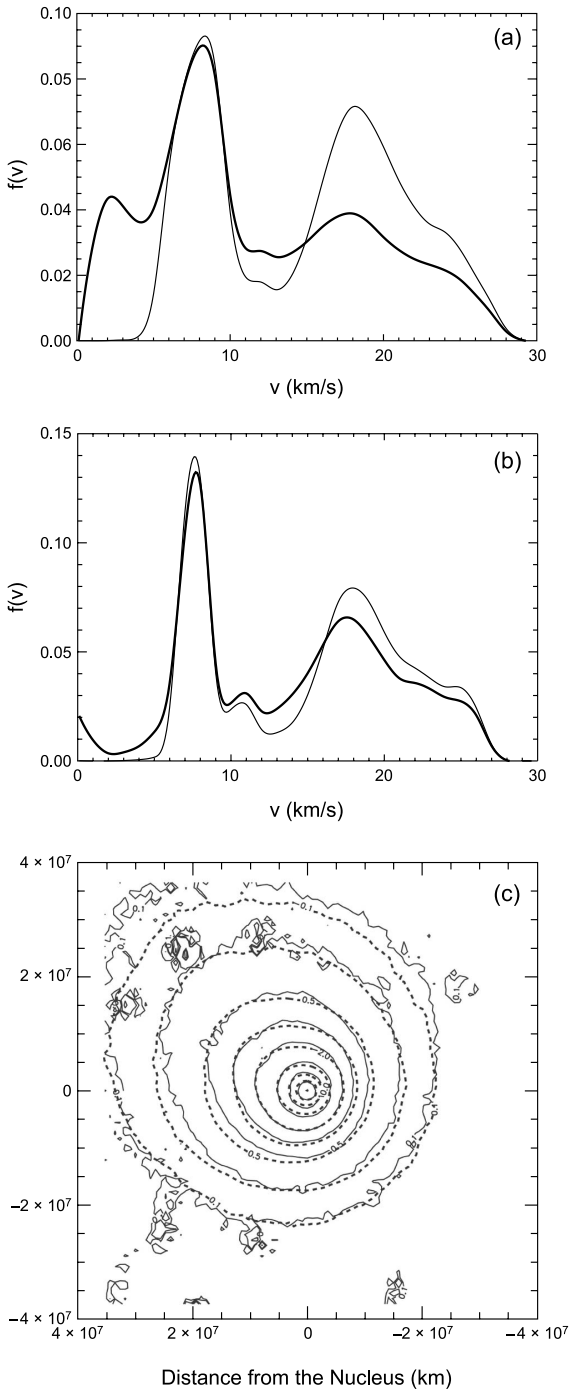

Fig. 9. Model for the SOHO SWAN observations of the H Lyman-α coma of Comet 1995 O1 (Hale-Bopp); **(a)** and **(b)** show the H-atom velocity distribution upon photochemical production (thin) and after Monte Carlo model calculation (thick) of thermalization in an expanding water-dominated coma. **(a)** Conditions on the day of perihelion (April 1, 1997) when the comet was at a heliocentric distance of 0.91 AU and the water production rate was 1.02×10^{31} s^{-1}. **(b)** Conditions on January 1, 1997 when these values were 1.75 AU and 2.2×10^{30} s^{-1} respectively. **(c)** The model-data comparison for the H coma at perihelion on April 1 when collisional thermalization was the largest and the resulting coma is the most distorted from spherical symmetry. The shape of the coma is formed by the balance between solar radiation pressure acceleration and the velocity distribution function.

and three months earlier (1.7 AU), when the production rate was much lower and the dissociation rates much lower. Near perihelion a large fraction of the highest-speed H atoms are thermalized to much lower velocities than at 1.7 AU where the distribution was not changed much. The effects of thermalization are directly evident in the perihelion Hα line-profile measurements of *Morgenthaler et al.* (2002). As discussed earlier, this slowing of the H atoms in Hale-Bopp is matched by a corresponding increase in the outflow speed of the heavy species, to which the kinetic energy is being transferred. Both *Harris et al.* (2002) and *Colom et al.* (1999) see clear evidence of this effect in the velocity structure of OH near Hale-Bopp's perihelion. The shape of the coma at perihelion, as shown in Fig. 9c and as observed with the SWAN instrument on SOHO, is also sensitive to the velocity distribution as first pointed out by *Keller and Meier* (1976).

The calculation of the water production rates (or any species for that matter), from either fast species like H or slower heavier species like OH or water, is very sensitive to our knowledge of the velocity distribution, unless the full scale length is observed (see equation (26)). This complication is substantially magnified by the multiple, radially dependent components of the H velocity distribution and by the large spatial extent of the H coma. At present we are able to sample spectrally only small, discrete subsets of the coma in the UV (H Lyman-α) or large azimuthally and radially averaged areas at moderate signal to noise (*Morgenthaler et al.,* 2002). Improvements in interferometric instrument capabilities in the FUV (*Stephan et al.,* 2001) and visible offer the promise of additional spatial information and increased spectral resolution for future comets. Other new diagnostics, including observations in the deep FUV (H Lyman-β) from FUSE (*Feldman et al.,* 2002), measurements of Hβ emission from Comet C/1996 B2 (Hyakutake) (*Scherb et al.,* 1996), and the planned STEREO (SOHO follow-up) mission, suggest a greater capability to map the structure of the H coma in future comets.

5.2.3. O(^{1}D) diagnostics. Oxygen in the metastable ^{1}D state is a byproduct of H_2O, OH, and CO photochemistry that is produced at different rates across the coma. Relaxation of O(^{1}D) produces a single photon ~110 s after its formation, meaning that its brightness inverts directly to its combined parent production rate without any supplemental knowledge of g-factors via equation (27) above. Only the various parent lifetimes and chemical branching ratios are required to complete the inversion, and, if the full O coma is sampled, the lifetime dependence disappears as well. Its short lifetime of the metastable state offers an additional advantage, because the locations of formation and emission are nearly co-local. Thus, the radial distribution of O(^{1}D) is a radial map of the site of photochemistry in the coma that is useful for detailed modeling of chemical rates, source distributions, and the relative density ratio of H_2O and CO.

Observations of O(^{1}D) do have significant complications as a proxy for H_2O and OH photochemistry that are addressable to a large degree. Observationally, these complications

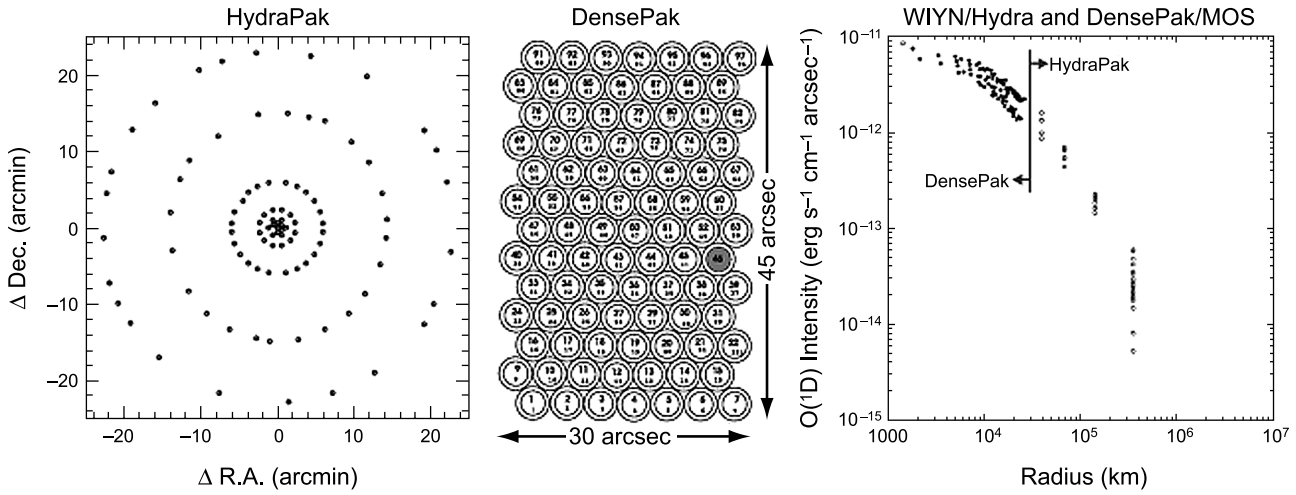

Fig. 10. Two types of multiport spectroscopy and their application to Comet Hale-Bopp are shown (from *Morgenthaler et al.,* 2001). At left is a sample distribution using the Hydra spectrograph on the WIYN telescope. Here a set of 100 fibers are placed at programmed positions over a 1° FOV with a minimum separation of 40 arcsec. The array design shown is optimized for the study of radially distributed emission, with the individual fibers feeding a bench spectrograph mounted below the telescope pier. At center is a schematic of DensePak, a tight grouping of 100 fibers covering a region equal the minimum spacing in the Hydra array. At right is an example of observation of O(1D) from Hale-Bopp using DensePak in the inner coma and Hydra for more remote locations.

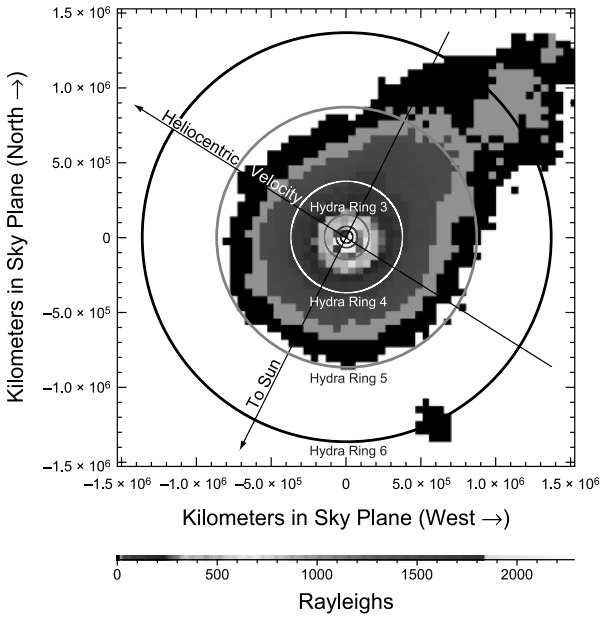

Fig. 11. A single 1° field image slice of the O(1D) coma of Hale-Bopp is shown after subtraction of continuum. This image was obtained using the WHαM instrument at Kitt Peak (from *Morgenthaler et al.,* 2001). Overlaid is the location of fiber rings from the Hydra instrument using the array shown in Fig. 8.

include substantial telluric O(1D) nightglow, spectral separation of O I and nearby NH_2 and H_2O^+ coma lines (see *Feldman et al.,* 2004), and the low contrast of the emission over bright dust scattered continuum emission. Physical complications include an unknown contribution from CO photochemistry that can be partially correctable with observations of C(1D) (see below) (*Oliversen et al.,* 2002), uncertainty in the branching ratios from OH under different levels of solar activity (*van Dishoeck et al.,* 1984; *Huebner et al.,* 1992; *Morgenthaler et al.,* 2001), UV opacity effects on chemical rates, and the role of collisional quenching and chemistry of O(1D) in the inner coma (*Glinsky et al.,* 2003; *Komitov,* 1989). To compensate for the observational effects, O(1D) is now routinely observed using high-spectral-resolution (R > 15000) techniques including long-slit echelle spectroscopy (*Fink and Hicks,* 1996), multiplexed echelle spectroscopy (Fig. 10) (*Anderson,* 1999), interferometric data cube imaging (Fig. 11), and aperture summed line measurements (Fig. 12). The recent detection of fluorescence of metastable O I (D^1-D^1) by FUSE (*Feldman et al.,* 2002) offers a potential new diagnostic that is comparable to the C(1D) line (see below).

As noted above, the integrated brightness of O(1D) is invertable to a production rate with equation (27) and from there to Q_{H_2O} from the branching ratios of OH and H_2O photochemistry. The radial and azimuthal distribution of the emission traces both the expansion of the coma and the rate of collisional and chemical quenching in the inner coma. Because it maps directly to chemistry, O(1D) images also reveal extended sources and regions of increased velocity (*Morgenthaler et al.,* 2002). The O(1D) outflow velocity retains the value of its parents (~1–2 km/s) plus fixed isotropic speed component of about 1.6 or 1.5 km/s from the photochemical excess energy from H_2O and OH, respectively. This requires high resolution ($R < 10^5$) to detect. This was achieved for 1P/Halley in 1986, with a Fabry-Pérot interferometer tuned to $R = 1.9 \times 10^5$ (Fig. 12), although it

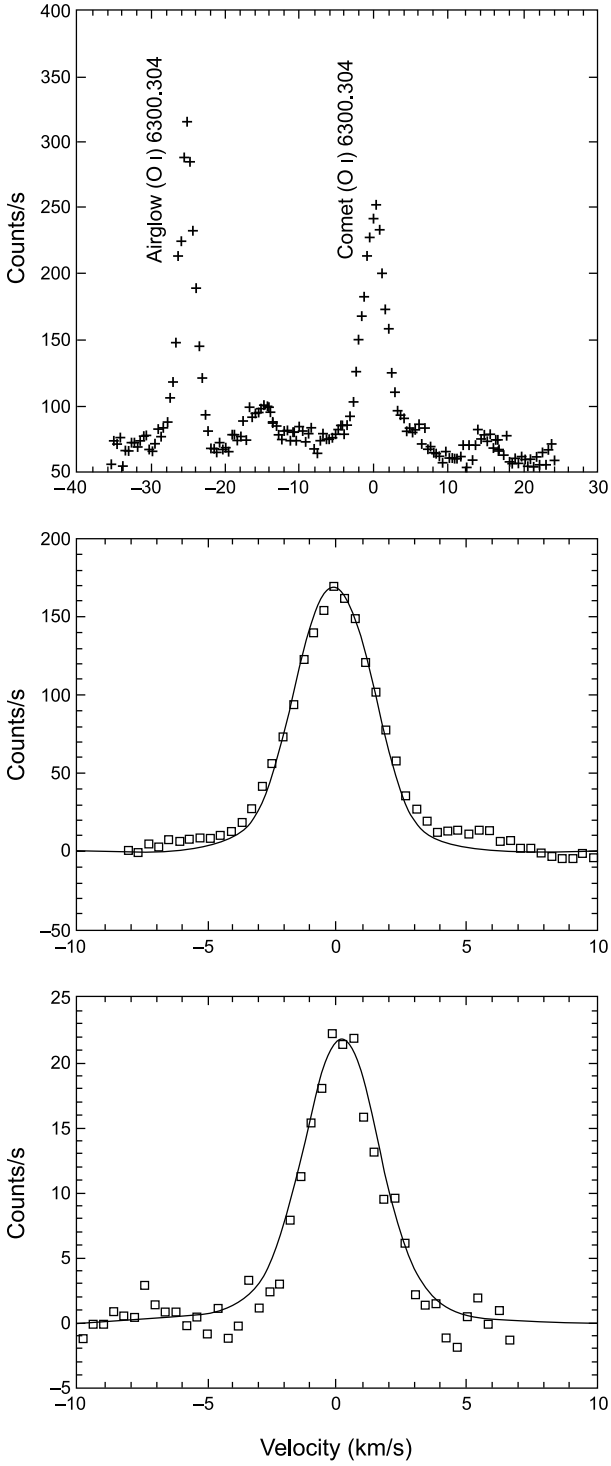

Fig. 12. Aperture-summed O(¹D) emission from 1P/Halley is displayed at the top showing the clean separation of comet and airglow O(¹D) signatures from each other and cometary NH_2 emission. These were obtained using a Fabry-Pérot interferometer in ring mode. Inspection of the comet and telluric line shapes shows the broadening in the Halley outflow. The lower panels show that this broadening is consistent with the magnitude of coma outflow predicted by model calculations to be broader at smaller (middle panel) heliocentric distances and more narrow at larger (bottom panel) distances (*Smyth et al.,* 1995).

required the averaging of a substantial FOV to obtain acceptable s/n on the line-shape. The Halley profiles were fit successfully using the Monte-Carlo particle trajectory model of *Combi et al.* (1993) and were used to validate the model-predicted magnitude of expansion velocity and its increase with increasing gas production (*Smyth et al.,* 1995). Observations of a similar resolution were made of the inner coma O(¹D) distribution with a high-resolution echelle spectrometer of Comet C/1996 B2 (Hyakutake). These were also in agreement with model predictions for conditions intermediate between the two Halley cases (*Combi et al.,* 1999a). Continued development of very-high-resolution interferometric techniques and sensitive high-resolution echelle instruments will make such observational programs routine for comets of moderate to high activity, while the further development of FUSE band technology may provide a complementary diagnostic that will provide useful results for weaker comets.

5.2.4. Infrared and radio observations of H_2O. A missing key to the observational study of water dynamical and photochemical evolution is measurement of the properties of the parent species. This has been historically difficult both because of the lack of transitions in the FUV-visible band and because of strong attenuation of IR and radio bands by telluric water. Over the past two decades considerable progress has been made in finding ways around the telluric problem by moving to spacebased observatories or by observing within the various windows where atmospheric absorption is not so severe. Comets can sometimes be observed at large enough geocentric velocity in order to Doppler shift the cometary feature away from terrestrial absorption features. These improvements offer considerable promise that spacebased aperture photometry of water in the radio will become routine, while IR measurements (both ground- and spacebased) will contribute both the temperature and radial distribution of water. Together they will fill an important observational niche in our study of coma kinetics. The issue of observations of H_2O, and parent molecules in general, is covered in detail in *Bockelée-Morvan et al.* (2004).

Unambiguous detection of water in the inner coma first came from 1P/Halley via the Kuiper Airborne Observatory (KAO) (*Mumma et al.,* 1986) and the IKS instrument on the *Vega* spacecraft (*Combes et al.,* 1986), both of which directly detected emission lines from the ν_3 band near 2.65 μm. In addition to providing a direct measurement of H_2O, the KAO data were used to derive both the nuclear spin temperature (T_{spin}) (*Mumma et al.,* 1987) and the rotational temperature (T_{rot}) (*Bockelée-Morvan and Crovisier,* 1987) of the lines, which sample the formation history and the current state of water in the coma respectively. The spin temperature derived from the ortho-para ratio on the different detected lines of the ν_3 band is set at the creation of the H_2O molecule by either photochemistry or direct evaporation from ice on the nucleus and thus directly ties to that event. The results from 1P/Halley ($N_{ortho}/N_{para} = 2.66 \pm 0.13$ indicating T_{spin} = 32 K +5, –2) were consistent with the

predicted temperature at the surface of Halley's nucleus at aphelion. Inversion of rotational state population to temperature is less straightforward because the H_2O molecules are IR pumped and strongly non-LTE, with a varying rate of neutral-neutral and neutral-electron collisions playing a significant role in the level population. Within these limitations, the rotational temperatures derived (T_{rot} ~60 K for the March 1986 KAO data) suggest that the kinetic temperature, as also reproduced in hybrid/gas-dynamic models (*Combi,* 1989), is also similarly low in the region of the coma sampled.

An area where considerable progress has been made is in the inversion of H_2O brightness to Q_{H_2O} and its spatial and temporal variance. *Weaver et al.* (1987) derived Q_{H_2O} from the same ν_3 KAO data used to derive T_{spin} and T_{rot}, obtaining results similar to OH, but with far greater variability on both short and long timescales. They attributed the short-term effects to a parent species sensitivity to nucleus activity that had previously been identified in CS (*McFadden et al.,* 1987), but could not fully account for the longer-term discrepancies. Finally, while they lacked the spectral resolution to sample the velocity structure of the ν_3 lines directly, *Larson et al.* (1987) showed that gas production asymmetry provides a signature of outflow in the form of a Doppler term in the lines. Their post-perihelion measurements showed considerable variation from canonical assumptions of water outflow consistent with collisional heating in active comets that was subsequently shown more dramatically in C/1995 O1 (Hale-Bopp) (*Harris et al.,* 2002).

Subsequent observations of water production and temperature using this ν_3 band and rotational lines near 180 μm have been made with the Infrared Space Observatory (ISO) satellite (*Crovisier et al.,* 1997) with results similar to those of the KAO and IKS IR spectrometer onboard in the *Giotto* spacecraft. In addition, *Dello Russo et al*. (2000) has used the CSHELL instrument at NASA IRTF to demonstrate a method for groundbased detection of water in nonresonance fluorescence "hot-bands" that are not absorbed by the atmosphere. These were first confirmed in Comet 1P/Halley (e.g., *Weaver et al.,* 1987.) Unlike other studies, the CSHELL measurements are spatially resolved over the small aperture of the instrument, providing the first radial maps of the inner coma water distribution and an opportunity to apply production models to identify both collisional effects and the presence of an extended source.

Progress in the study of line-resolved aperture photometry of the water band at 557 GHz, which are available only from space platforms, has proven very useful for deriving Q_{H_2O} and V_{H_2O} from the line shape. This emission was first detected from Comet C/1991 H1 (Lee) using the Submillimeter Wave Astronomy Satellite (SWAS) (*Neufeld et al.,* 2000), and subsequently from Comets C/2001 A2 (LINEAR), 19P/Borrelly, C/2000 WM1 (LINEAR), and 153P/2002 C1 (Ikeya-Zhang) with the Odin satellite. The radio measurements suffer from the same large area summation as those used to examine other species; however, they share their primary strength, velocity sensitivity. The Odin instrumental resolution is sufficiently high (80 m/s) to fully resolve the ~1 km s^{-1} bulk flow of water, which can now be compared with similar measurements of other water daughters (H and OH) over similar FOV and used to model the complex kinetics of the coma in the active comets detectable with these techniques.

5.3. Water Diagnostics in the Far-Ultraviolet (Far Ultraviolet Spectroscopic Explorer) Bandpass

The launch of FUSE opened a new chapter in comet studies by enabling direct observation of new diagnostics of water production and chemistry in the FUV. To date, FUSE has been used to observe long-period Comets C/1999 T1 (McNaught-Hartley), C/2000 WM1 (LINEAR), and C/2001 A2 (LINEAR) (*Feldman et al.,* 2002; *Weaver et al.,* 2002). In addition to putting new limits on the abundance fraction of highly volatile species such as Ar (*Weaver et al.,* 2002) and CO (*Feldman et al.,* 2002), several diagnostic features identified with water photochemistry have been observed. These include the H_2 Lyman band lines at 1071.6, 1118.6, and 1166.8 Å, H Lyman-β and other lines of the Lyman series, O I multiplets at 989, 1027, and 1040 Å, fluorescence from the metastable O I(^{1}D) state at 1152 Å [analogous to the more commonly studied C(^{1}D) emission line at 1931 Å (*Tozzi et al.,* 1998)] (*Feldman et al.,* 2002), and the possible detection of charge exchange (between coma neutrals and the high ionization state component of the solar wind) cascade lines of O IV at 1031.93 and 1037.62 Å (*Weaver et al.,* 2002).

The utility of these new diagnostics is still being evaluated; however, it is promising that the two objects observed to date have been intrinsically weak gas producers that would yield poor results with many of the other techniques described above. Detection of H_2 is significant in that it provides a new diagnostic of the poorly studied branching rate to that daughter from water. H_2 is also produced with a substantial excess velocity (Table 2) and has a long lifetime against photodissociation (Table 4), a combination that means that, while H_2 is a minor inner coma constituent, it is a dominant molecule in the outer coma. *Feldman et al.* (2002) suggest that the O(^{1}D–^{0}D) resonance is being stimulated by an unknown process rather than fluorescing in the comet inner coma. This result is somewhat enigmatic, considering that fluorescence is the dominant source of C(^{1}D) in the coma despite having a lower energy of transition than O(^{1}D). Whether the O(^{1}D) results for the three comets studied is typical or an anomaly brought about by the unique circumstances of the FUSE observations (e.g., aperture, solar cycle, low intrinsic production rates) will require a larger dataset and close theoretical scrutiny to determine.

The major limitations for working in the FUV bandpass are the availability of observing time, only moderately high spectral resolution, high sky background noise, the relatively low level of solar FUV flux, and the 30" × 30" angular extent of its aperture, which combine to limit observations to the inner coma. In this regard FUSE has similar limitations to IUE in the 1980s and 1990s. As in this earlier case, the advent of larger aperture and more flexible instru-

ments will improve our ability to monitor these important new features.

5.4. The Relationship of Other Coma Species to Water

Water is the dominant volatile component of comet nuclei, and therefore its state and evolution are both relevant to developing an understanding of other coma species, some of which have reciprocal effects on the water coma. The above descriptions reveal several weaknesses in the diagnostics suite used to determine the characteristics of the water coma, and one technique to address this is to combine studies of water with other coma constituents that fill these observational voids. The detailed physics of the other coma species is dealt with in other chapters of this book, and our goal here is to illustrate only how a coordinated observing-modeling approach between them and water will increase our understanding of each. While coordinated observations of multiple species provide benefits for understanding many other properties of the coma, including its thermal properties and the interaction of the solar wind, we will briefly touch here on two examples (the velocity structure of the inner coma and the role of secondary sources of water daughter species) where the above techniques provide an incomplete picture and observational solutions using other species have been identified.

5.4.1. Velocity structure. The low velocity of most coma constituents (in particular, H_2O, OH, and O for water) requires extremely high spectral resolution ($R > 10^5$) to measure. Unfortunately, the most common technique used to achieve such high resolution in the visible and UV (echelle spectroscopy) has a correspondingly small étendue that samples only small regions with fairly low sensitivity. Interferometric techniques (*Stephan et al.,* 2001; *Watchorn et al.,* 2001; *Morgenthaler et al.,* 2002) that co-add large FOV at high spectral resolution in the visible and UV have considerable future promise in this area; however, the most mature techniques exist in the radio. Unfortunately, the primary water diagnostic in the radio (OH at 18 cm) is strongly quenched in the inner coma, which is its the most dynamically active region for active comets. To get around this problem it is possible to use other, less-quenched OH [e.g., IR (*Crovisier et al.,* 1997)] emission features or other species to study this region and combine the results to complete the dynamical picture. Several such features exist and are in common use to determine the velocity within ~10^3–10^4 km of the nucleus (*Biver et al.,* 1999b). One commonly observed emission that is useful for such comparative work is the J = 1–0 line of HCN (*Schloerb et al.,* 1987; *Biver et al.,* 1999b), which is detectable close to the nucleus at subkilometers per second velocity resolution and therefore useful in coordination with OH to measure velocity in the inner and outer coma. Models of the outflow (*Combi,* 1989) similar to those shown in Figs. 3–6 reproduced the secular variation (with heliocentric distance) of the HCN line width seen by *Schloerb et al.* (1987). *Harris et al.* (2002) combined published measurements of the outer coma OH velocity (*Colom et al.,* 1999) and inner coma HCN velocity (*Biver et al.,* 1999a) with the radial distribution of emission from OH to map out the acceleration across the coma of C/1995 O1 (Hale-Bopp). The magnitude and variation of these velocity measurements, both with distance from the nucleus and overall with heliocentric distance, are also in reasonable agreement with models for the expansion of the coma (*Combi et al.,* 1999b), even for the extreme physical state of Hale-Bopp.

5.4.2. Characterization secondary sources. Of the primary neutral water species only H_2O itself and OH have no significant contribution from other sources. Of the others, O I has the largest nonwater component, in this case from a combination of CO and CO_2. The precision of model interpretation of O(^{1}D) will depend on the precision by which the CO- and H_2O-derived components are separated or by our knowledge of the CO/H_2O ratio, which varies substantially among comets and with heliocentric distance. The size of the CO/CO_2 contribution can be dominant in the outer solar system, where water outgassing is suppressed, but even where water dominates, the addition of CO/CO_2-derived O [particularly O(^{1}D)] is significant. The role of CO/CO_2 is further complicated by the fact that the rate of formation of O(^{1}D) differs between the two species and with respect to both pathways in water. Indeed, O(^{1}D), derived from CO (as a daughter) and CO_2 (as a granddaughter), most likely dominates over the OH contribution in the outer coma due to the longer lifetime of CO (*Tozzi et al.,* 1998; *Harris et al.,* 1999). This would be even further complicated by a substantial fraction of CO coming from an extended source of another parent like H_2CO (*DiSanti et al.,* 2001). Moreover, the ratios of $CO : CO_2$, CO/H_2O, and $CO_2 : H_2O$ vary substantially between comets, with no obvious predictive trend yet identified (*Weaver et al.,* 1994; *Feldman et al.,* 1997; see also *Bockelée-Morvan et al.,* 2004). Thus, to account for the contribution of these species to the O(^{1}D) brightness and spatial distribution, it is necessary to study diagnostics of both CO and CO_2 chemistry. The most direct method is to study C(^{1}D), the metastable analog to O(^{1}D) that is formed in the same process from CO (*Huebner et al.,* 1992; *Tozzi et al.,* 1998). From $Q_{C(^1D)}$ it is possible to separate the CO and OH contributions directly over any simultaneously observed FOV.

There are two diagnostics for C(^{1}D): fluorescence from the ^{1}D state at 1931 Å and direct detection of the C(^{1}D) decay at 9828/9850 Å. The former is accessible only from space and has typically been studied only over small FOV (*Feldman et al.,* 1997), which limits its usefulness for a full coma correction. Direct observation of the NIR decay lines holds more promise, because it is both directly analogous to the O I visible line and observable from the ground. This feature is faint compared to O(^{1}D), has high background contamination, and falls near a telluric OH absorption. It has only been detected in two comets, first an unpublished detection from 1P/Halley by *Münch et al.* (1986), and more recently from Fabry-Pérot interferometric observations of C/1995 O1 Hale-Bopp (*Oliversen et al.,* 2002). The Hale-Bopp detection provides the first quantitative estimates of

the role of C(^{1}D) in the inner and outer coma and identifies how future development of the interferometric technique will improve our ability to study this diagnostic.

6. OUTSTANDING ISSUES AND FUTURE STUDIES OF COMA STRUCTURE AND EXPANSION

There is currently no single diagnostic signature of water that provides a complete description of its spatial, velocity, temporal, and production rate evolution in the coma. Inferring such detail from any one observation therefore requires either an estimate or approximation of the unknown quantities (usually from observed characteristics of earlier comets) or model derivation of them. As the quality of remote sensing data has improved, the limiting factor in interpretation has shifted from the instrumental regime to the degree to which we know (1) underlying physical parameters such as g-factors and rate constants; (2) internal factors including quenching, temperature, solar wind density and velocity, collision rates, optical depth, and source distribution; (3) incoming solar spectral intensity in the UV; (4) parent species' contributions and branching ratios; and (5) the two-dimensional and temporal structure of the coma and how it effects observations taken over different spatial scales or at different times.

To the extent that these parameters are known for each case, the modeling techniques discussed here each provide a consistent picture of water evolution from the observations. However, one effect of this shift is that the precision of measurements now often greatly exceeds the accuracy of the inverted result (*Schleicher et al.,* 1998). In many cases the divergence between different methods stems more from the failure to fully account for this in the determination of uncertainty than from the validity of the approach, and can give the impression of nonconvergence when isolated observations are compared directly. Another major effect is the inversion or synthetic reproduction of data with spherical and/or steady-state models. Not accounting for such complicating effects can result in erroneously attributing features in the data to those free parameters that are left in the model. Finally, in the absence of simultaneous *in situ* data from multiple spacecraft, we are always left with the projection of all information (spatial, velocity, and temperature) along the line of sight that again can result in similar misinterpretations.

A clear improvement of the model fits is obtained when multiple diagnostics with synergistic results and unknowns are combined, particularly if they are obtained nearly simultaneously and can account for temporal and spatial variances. For example, the combination of wide-field (production rate) and velocity-resolved (outflow and nonthermal components) aperture photometry of a species with two-dimensional spatial imaging (parent-daughter scale lengths, azimuthal structure, propagating temporal activity changes) provides a set of reciprocal boundary values for the individual uncertainties in each observation. Where this approach has been applied, it has significantly reduced the allowed parameter space of the converged model for the coma (*Combi et al.,* 2000; *Morgenthaler et al.,* 2001; *Harris et al.,* 2002). The caveat to this is that the capability to perform the required observations is widely distributed and is typically organized only for high-profile apparitions (e.g., 1P/Halley, C/1995 O1 Hale-Bopp, C/1996 B2 Hyakutake). The results of these campaigns suggest that an improvement in our understanding of both the role of water in the coma and in the physical parameters that describe its evolution would result from a consistent organized effort targeting a larger sample of comets covering a wider range of activity and evolution.

Acknowledgments. M.R.C. acknowledges support from grant NAG5-13239 from the NASA Planetary Atmospheres program.

REFERENCES

A'Hearn M. F., Hoban S., Birch P. V., Bowers C., Martin R., and Klinglesmith D. A. III (1986) Cyanogen jets in Comet Halley. *Nature, 324,* 649–651.

Allen M., Delitsky M., Huntress W., Yung Y., and Ip W.-H. (1987) Evidence for methane and ammonia in the coma of Comet P/Halley. *Astron. Astrophys., 187,* 502–512.

Anderson C. M. (1999) Fiberoptically multiplexed medium resolution spectroscopy from the WIYN telescope, singlet D neutral oxygen, NH_2, and H_2O^+. *Earth Moon Planets, 78,* 99–104.

Bertaux J.-L. and Lallement R. (1984) Analysis of interplanetary Lyman-alpha line profile with a hydrogen absorption cell — Theory of the Doppler angular spectral scanning method. *Astron. Astrophys., 140,* 230–242.

Biver N., Bockelée-Morvan D., Colom P., Crovisier J., Germain B., Lellouch E., Davies J. K., Dent W. R. F., Moreno R., Paubert G., Wink J., Despois D., Lis D. C., Mehringer D., Benford D., Gardner M., Phillips T. G., Gunnarsson M., Rickman H., Winnberg A., Bergman P., Johansson L. E. B., and Rauer H. (1999a) Long-term evolution of the outgassing of Comet Hale-Bopp from radio observations. *Earth Moon Planets, 78,* 5–11.

Biver N., Bockelée-Morvan D., Crovisier J., Davies J. K., Matthews H. E., Wink J. E., Rauer H., Colom P., Dent W. R. F., Despois D., Moreno R., Paubert G., Jewitt D., and Senay M. (1999b) Spectroscopic monitoring of Comet C/1996 B2 (Hyakutake) with the JCMT and IRAM radio telescopes. *Astron. J., 118,* 1850–1872.

Biver N., Bockelée-Morvan D., Colom P., Crovsier J., Henry F., Lellouch E., Winnberg A., Johansson L. E. B., Cunnarsson M., Rickman H., Rantakyrö F., Davies J. K., Dent W. R. F., Paubert G., Moreno R., Wink J., Despois D., Benford D. J., Gardner M., Lis D. C., Mehringer D., Phillips T. G., and Rauer H. (2002) The 1995–2002 long-term monitoring of Comet C/1995 O1 (Hale-Bopp) at radio wavelength. *Earth Moon Planets, 90,* 5–14.

Bird G. A. (1994) *Molecular Gas Dynamics and the Direct Simulation of Gas Flows.* Clarendon, Oxford. 459 pp.

Bockelée-Morvan D. (1987) A model for the excitation of water in comets. *Astron. Astrophys., 181,* 169–181.

Bockelée-Morvan D. and Crovisier J. (1987) The role of water in the thermal balance of the coma. In *Proceedings of the Symposium on the Diversity and Similarity of Comets* (E. J. Rolfe and B. Battrick, eds.), pp. 235–240. ESA SP-278, Noordwijk, The Netherlands.

Bockelée-Morvan D., Crovisier J., and Gerard E. (1990) Retrieving the coma gas expansion velocity in P/Halley, Wilson (1987 VII) and several other comets from the 18-cm OH line shapes. *Astron. Astrophys., 238,* 382–400.

Bockelée-Morvan D., Crovisier J., Colom P., and Despois D. (1994) The rotational lines of methanol in Comets Austin 1990 V and Levy 1990 XX. *Astron. Astrophys., 287,* 647–665.

Bockelée-Morvan D., Crovisier J., Mumma M. J., and Weaver H. A. (2004) The composition of cometary volatiles. In *Comets II* (M. C. Festou et al., eds.), this volume. Univ. of Arizona, Tucson.

Brooke T. Y., Tokunaga A. T., Weaver H. A., Crovisier J., Bockelée-Morvan D., and Crisp D. (1996) Detection of acetylene in the infrared spectrum of Comet Hyakutake. *Nature, 383,* 606–608.

Brooke T. Y., Weaver H. A., Chin G., Bockelée-Morvan D., Kim S. J., and Xu L.-H. (2003) Spectroscopy of Comet Hale-Bopp in the infrared. *Icarus, 166,* 167–187.

Budzien S. A., Festou M. C., and Feldman P. D. (1994) Solar flux variability of cometary H_2O and OH. *Icarus, 107,* 164–188.

Chin G. and Weaver H. A. (1984) Vibrational and rotational excitation of CO in comets. Nonequilibrium calculations. *Astrophys. J., 285,* 858–869.

Cochran A. L. (1985) A re-evaluation of the Haser model scale lengths for comets. *Astron. J., 90,* 2609–2514.

Cochran A. L. and Schleicher D. G. (1993) Observational constraints on the lifetime of cometary H_2O. *Icarus, 105,* 235–253.

Colom P., Gerard E., Crovisier J., Bockelée-Morvan D., Biver N. and Rauer H. (1999) Observations of the OH radical in Comet C/1995 O1 (Hale-Bopp) with the Nançay radio telescope. *Earth Moon Planets, 78,* 37–43.

Combes M., Moroz V., Crifo J.-F., Lamarre J. M., Charra J., Sanko N. F., Soufflot A., Bibring J. P., Cazes S., Coron N., Crovisier J., Emerich C., Encrenaz T., Gispert R., Grigoryev A. V., Guyot G., Krasnopolsky V. A., Nikolsky Yu. V., and Rocard F. (1986) Infrared sounding of Comet Halley from Vega 1. *Nature, 321,* 266–268.

Combi M. R. (1987) Sources of cometary radicals and their jets — Gases or grains. *Icarus, 71,* 178–191.

Combi M. R. (1989) The outflow speed of the coma of Halley's comet. *Icarus, 81,* 41–50.

Combi M. R. (1996) Time-dependent gas kinetics in tenuous planetary atmospheres: The cometary coma. *Icarus, 123,* 207–226.

Combi M. R. (2002) Hale-Bopp: What makes a big comet different. Coma dynamics: Observations and theory. *Earth Moon Planets, 89,* 73–90.

Combi M. R. and Delsemme A. H. (1980) Neutral cometary atmospheres. I. Average random walk model for dissociation in comets. *Astrophys. J., 237,* 633–641.

Combi M. R. and Fink U. (1993) P/Halley — Effects of time-dependent production rates on spatial emission profiles. *Astrophys. J., 409,* 790–797.

Combi M. R. and Fink U. (1997) A critical study of molecular photodissociation and CHON grain sources for cometary C. *Astrophys. J., 484,* 879–890.

Combi M. R. and Smyth W. H. (1988a) Monte Carlo particle trajectory models for neutral cometary gases. I. Models and equations. *Astrophys. J., 327,* 1026–1043.

Combi M. R. and Smyth W. H. (1988b) Monte Carlo particle trajectory models for neutral cometary gases. II. The spatial morphology of the Lyman-alpha coma. *Astrophys. J., 327,* 1044–1059.

Combi M. R., Bos B. J., and Smyth W. H. (1993) The OH distribution in cometary atmospheres — A collisional Monte Carlo model for heavy species. *Astrophys. J., 408,* 668–677.

Combi M. R., Brown M. E., Feldman P. D., Keller H. U., Meier R. R., and Smyth W. H. (1998) Hubble Space Telescope ultraviolet imaging and high-resolution spectroscopy of water photodissociation products in Comet Hyakutake (C/1996 B2). *Astrophys. J., 494,* 816–821.

Combi M. R., Cochran A. L., Cochran W. D., Lambert D. L., and Johns-Krull C. M. (1999a) Observation and analysis of high-resolution optical line profiles in Comet Hyakutake (C/1996 B2). *Astrophys. J., 512,* 961–968.

Combi M. R., Kabin K., DeZeeuw D. L., Gombosi T. I., and Powell K. G. (1999b) Dust-gas interrelations in comets: Observations and theory. *Earth Moon Planets, 79,* 275–306.

Combi M. R., Reinard A. A., Bertaux J.-L., Quemerais E., and Mäkinen T. (2000) SOHO/SWAN observations of the structure and evolution of the hydrogen Lyman-alpha: Coma of Comet Hale-Bopp (1995 O1). *Icarus, 144,* 191–202.

Cravens T. E., Kozyra J. U., Nagy A. F., Gombosi T. I., and Kurtz M. (1987) Electron impact ionization in the vicinity of comets. *J. Geophys. Res., 92,* 7341–7353.

Crifo J.-F., Crovisier J., and Bockelée-Morvan D. (1989) Proposed water velocity and temperature radial profiles appropriate to comet Halley flyby conditions. Paper presented at the 121st Colloquium of the International Astronomical Union, held in Bamberg, Germany, April 24–28, 1989.

Crifo J.-F., Itkin A. L., and Rodionov A. V. (1995) The near-nucleus coma formed by interacting dusty gas jets effusing from a cometary nucleus: I. *Icarus, 116,* 77–112.

Crifo J.-F., Rodionov A. V., and Bockelée-Morvan D. (1999) The dependence of the circumnuclear coma structure on the properties of the nucleus. *Icarus, 138,* 85–106.

Crifo J.-F., Lukianov G. A., Rodionov A.V., Khanlarov G. O., and Zakharov V. V. (2002) Comparison between Navier-Stokes and direct Monte-Carlo simulations of the circumnuclear coma. I. Homogeneous, spherical source. *Icarus, 156,* 249–268.

Crifo J.-F., Loukianov G. A., Rodionov A. V., and Zakharov V. V. (2003) Navier-Stokes and direct Monte Carlo simulations of the circumnuclear coma II. Homogeneous, aspherical sources. *Icarus, 163,* 479–503.

Crifo J.-F., Kömle N. I., Fulle M., and Szegö K. (2004) Nucleus-coma structural relationships: Lessons from physical models. In *Comets II* (M. C. Festou et al., eds.), this volume. Univ. of Arizona, Tucson.

Crovisier J. (1984) The water molecule in comets: Fluorescence mechanisms and thermodynamics of the inner coma. *Astron. Astrophys., 130,* 361–372.

Crovisier J. (1989) The photodissociation of water in cometary atmospheres. *Astron. Astrophys., 213,* 459–464.

Crovisier J., Leech K., Bockelée-Morvan D., Brooke T. Y., Hanner M. S., Altieri B., Keller H. U., and Lellouch E. (1997) The spectrum of Comet Hale-Bopp (C/1995 O1) observed with the infrared space observatory at 2.9 astronomical units from the Sun. *Science, 275,* 1904–1907.

Crovisier J., Colom P., Gérard E., Bockelée-Morvan D., and Bourgois G. (2002) Observations at Nançay of the OH 18-cm lines in comets. The data base. Observations made from 1982 to 1999. *Astron. Astrophys., 393,* 1053–1064.

Dello Russo N., Mumma M. J., DiSanti M. A., Magee-Sauer K., Novak R., and Rettig T. W. (2000) Water production and release in Comet C/1995 O1 Hale-Bopp. *Icarus, 143,* 324–337.

Delsemme A. H. and Miller D. C. (1971) The continuum of Comet

Burnham (1960 II): The differentiation of a short period comet. *Planet. Space Sci., 19,* 1229–1257.

DiSanti M. A., Mumma M. J., Dello Russo N., and Magee-Sauer K. (2001) Carbon monoxide production and excitation in Comet C/1995 O1 (Hale-Bopp): Isolation of native and distributed CO sources. *Icarus, 153,* 162–179.

Drake J. F., Jenkins E. B., Bertaux J.-L., Festou M., and Keller H. U. (1976) Lyman-alpha observations of Comet Kohoutek 1973 XII with Copernicus. *Astrophys. J., 209,* 302–311.

Eberhardt P., Krankowsky D., Schulte W. , Dolder U., Lämmerzahl P., Berthelier J. J., Woweries J., Stubbeman U., Hodges R. R., Hoffman J. H., and Illiano J. M. (1987) The CO and N_2 abundance in Comet P/Halley. *Astron. Astrophys., 187,* 481–484.

Eddington A. S. (1910) The envelopes of c 1908 (Morehouse). *Mon. Not. R. Astron. Soc., 70,* 442–458.

Fahr H. J. and Shizgal B. (1981) Modern exospheric theories and their observational relevance. *Rev. Geophys., 21,* 75–124.

Farnham T. L., Schleicher D. G., and A'Hearn M. F. (2000) The HB narrowband comet filters: Standard stars and calibrations. *Icarus, 147,* 180–204.

Feldman P. D., Festou M. C., Tozzi G. P., and Weaver H. A. (1997) The CO_2/CO abundance ratio in 1P/Halley and several other comets observed by IUE and HST. *Astrophys. J., 475,* 829–834.

Feldman P. D., Weaver H. A., and Burgh E. B. (2002) Far Ultraviolet Spectroscopic Explorer observations of CO and H_2 emission in Comet C/2001 A2 (LINEAR). *Astrophys. J. Lett., 576,* L91–L94.

Feldman P. D., Cochran A. L., and Combi M. R. (2004) Spectroscopic investigations of fragment species in the coma. In *Comets II* (M. C. Festou et al., eds.), this volume. Univ. of Arizona, Tucson.

Festou M. C. (1981a) The density distribution of neutral compounds in cometary atmospheres. I — Models and equations. *Astron. Astrophys., 95,* 69–79.

Festou M. C. (1981b) The density distribution of neutral compounds in cometary atmospheres. II — Production rate and lifetime of OH radicals in Comet Kobayashi-Berger-Milon /1975 IX/. *Astron. Astrophys., 96,* 52–57.

Festou M. C. (1999) On the existence of distributed sources in comet comae. *Space Sci. Rev., 90,* 53–67.

Festou M. C. and Feldman P. D. (1981) The forbidden oxygen lines in comets. *Astron. Astrophys., 103,* 154–159.

Fink U. and Hicks M. D. (1996). A survey of 39 comets using CCD spectroscopy. *Astrophys. J., 459,* 729–743.

Fink U., Combi M. R., and DiSanti M. A. (1991) Comet P/Halley — Spatial distributions and scale lengths for C_2, CN, NH_2, and H_2O. *Astrophys. J., 383,* 356–371.

Finson M. L. and Probstein R. F. (1968) A theory of dust comets. 1. Model and equations. *Astrophys. J., 154,* 327–352.

Fokker A. D. (1953) Some notes on the fountain model of cometary envelopes and streamers. *Mem. Sci. Liége, Ser. 4, 13,* 241–259.

Glinski R. J., Harris W. M., Anderson C. M., and Morgenthaler J. P. (2003) Oxygen/hydrogen chemistry in inner comae of active comets. In *Formation of Cometary Material,* 25th Meeting of the IAU, Joint Discussion 14, 22 July 2003, Sydney, Australia.

Gombosi T. I. (1994) *Gaskinetic Theory.* Cambridge Univ., Cambridge. 297 pp.

Gombosi T. I., Cravens T. E., and Nagy A. F. (1985) Time-dependent dusty gas dynamical flow near cometary nuclei. *Astrophys. J., 293,* 328–341.

Gombosi T. I., Nagy A. F., and T. E. Cravens (1986) Dust and neutral gas modeling of the inner atmospheres of comets. *Rev. Geophys., 24,* 667–700.

Grün E., Hanner M. S., Peschke S. B., Müller T., Boehnhardt H., Brooke T. Y., Campins H., Crovisier J., Delahodde C., Heinrichsen I., Keller H. U., Knacke R. F., Krüger H., Lamy P., Leinert C., Lemke D., Lisse C. M., Müller M., Osip D. J., Solc M., Stickel M., Sykes M., Vanysek V., and Zarnecki J. (2001) Broadband infrared photometry of Comet Hale-Bopp with ISOPHOT. *Astron. Astrophys., 377,* 1098–1118.

Häberli R., Combi M. R., Gombosi T. I., De Zeeuw D. L., and Powell K. G. (1997) Quantitative analysis of H_2O^+ coma images using a multiscale MHD model with detailed ion chemistry. *Icarus, 130,* 373–386.

Harlander J. M., Roesler F. L., Cardon J. G., Englert C. R., and Conway R. R. (2002) Shimmer: A spatial heterodyne spectrometer for remote sensing of Earth's middle atmosphere. *Applied Optics, 41,* 1343–1352.

Harmon J. K., Ostro S. J., Benner L. A. M., Rosema K. D., Jurgens R. F., Winkler R., Yeomans D. K., Choate D., Cormier R., Giogini J. D., Mitchell D. L., Chodas P. W., Rose R., Kelley D., Slade M. A., and Thomas M. L. (1997) Radar detection of the nucleus and coma of Comet Hyakutake (C/1996 B2). *Science, 278,* 1921–1924.

Harris W. M., Combi M. R., Honeycutt R. K., and Mueller B. E. A. (1997) Evidence for interacting gas flows and an extended volatile source distribution in the coma of Comet C/1996 B2 (Hyakutake). *Science, 277,* 676–681.

Harris W. M., Nordsieck K. H., Scherb F., and Mierkiewicz E. J. (1999) UV photopolarimetric imaging of C/1995 O1 (Hale-Bopp) with the Wide Field Imaging Survey Polarimeter (WISP). *Earth Moon Planets, 78,* 161–167.

Harris W. M., Scherb F., Mierkiewicz E. J., Oliversen R. J., and Morgenthaler J. P. (2002) Production, outflow velocity, and radial distribution of H_2O and OH in the coma of Comet C/1995 O1 [Hale-Bopp] from wide field imaging of OH. *Astrophys. J., 578,* 996–1008.

Haser L. (1957) Distribution d'intensite dans la tete d'une comete. *Bull. Acad. R. de Belgique, Classe de Sci. 43(5),* 740–750.

Hodges R. R. (1990) Monte Carlo simulation of nonadiabatic expansion in cometary atmospheres: Halley. *Icarus, 83,* 410–433.

Huebner W. F. (1985) The photochemistry of comets. In *The Photochemistry of Atmospheres: Earth, the Other Planets, and Comets* (J. S. Levine, ed.), pp. 437–481. Academic, Orlando.

Huebner W. F. and Carpenter C. W. (1979) *Solar Photo Rate Coefficients.* Los Alamos Sci. Lab. Report LA-8085-MS, Los Alamos National Laboratory, Los Alamos, New Mexico.

Huebner W. F. and Keady J. J. (1983) Energy balance and photochemical processes in the inner coma. In *Cometary Exploration, Vol. 1* (T. I. Gombosi, ed.), pp. 165–183. Central Research Institute for Physics, Budapest, Hungary.

Huebner W. F., Keady J. J., and Lyon S. P. (1992) Solar photo rates for planetary atmospheres and atmospheric pollutant. *Astrophys. Space Sci., 195,* 1–294.

Huppler D., Reynolds R. J., Roesler F. L., Scherb F., and Trauger J. (1975) Observations of Comet Kohoutek /1973f/ with a ground-based Fabry-Pérot spectrometer. *Astrophys. J., 202,* 276–282.

Ip W.-H. (1983) On photochemical heating of cometary comae: The cases of H_2O and CO-rich comets. *Astrophys. J., 264,* 726–732.

Ip W.-H. (1989) Photochemical heating of cometary comae.

III. The radial variation of the expansion velocity of CN shells in comet Halley. *Astrophys. J., 346,* 475–480.

Jackson W. M. (1976) Laboratory observations of the photochemistry of parent molecules: A review. In *The Study of Comets* (B. Donn et al., eds.), pp. 679–704. NASA SP-393, Washington, DC.

Jackson W. M. (1980) The lifetime of the OH radical in comets at 1 AU. *Icarus, 41,* 147–152.

Jewitt D., Senay M., and Matthews H. (1996) Observations of carbon monoxide in Comet Hale-Bopp. *Science, 271,* 1110–1113.

Kawakita H. and Watanabe J. (1998) NH_2 and its parent molecule in the inner coma of Comet Hyakutake (C/1996 B2). *Astrophys. J., 495,* 946–950.

Kawakita H., Watanabe J., Ando H., Alki W., Fuse T., Honda S., Izumiura H., Kajino T., Kambe E., Kawanaomoto S., Noguchi K., Okita K., Sadakane K., Sato B., Takada-Midai M., Takeda Y., Usunda T., Watanabe E., and Yoshinda M. (2001) The spin temperature of NH_3 in Comet C/1994 S4 (LINEAR). *Science, 294,* 1089–1091.

Keller H. U. and Meier R. R. (1976) A cometary hydrogen model for arbitrary observational geometry. *Astron. Astrophys., 52,* 273–281.

Keller H. U., Bohlin J. D., and Tousey R. (1975) High resolution Lyman alpha observations of Comet Kohoutek /1973f/ near perihelion. *Astron. Astrophys., 38,* 413–416.

Kiselev N. N. and Velichko F. P. (1999) Aperture polarimetry and photometry of Comet Hale-Bopp. *Earth Moon Planets, 78,* 347–352.

Kitamura Y. (1986) Axisymmetric dusty gas jet in the inner coma of a comet. *Icarus, 66,* 241–257.

Kitamura Y., Ashihara O., and Yamamoto T. (1985) A model for the hydrogen coma of a comet. *Icarus, 61,* 278–295.

Komitov B. (1989) The metastable oxygen O (^{1}D) as a possible source of OH molecules in the cometary atmospheres. *Adv. Space Res., 9,* 177–179.

Körösmezey A. and Gombosi T. I. (1990) A time-dependent dusty gas dynamic model of axisymmetric cometary jets. *Icarus, 84,* 118–153.

Krasnopolsky V. A. and 34 colleagues (1986a) The VEGA-2 TKS experiment — Some spectroscopic results for Comet Halley. *Soviet Astron. Lett., 12(4),* 259–262.

Krasnopolsky V. A. and 13 colleagues (1986b) Spectroscopic study of Comet Halley by the VEGA 2 three-channel spectrometer. *Nature, 321,* 269–271.

Kupperman D. G. (1999) Nonthermal atoms in planetary, satellite, and cometary atmospheres. Ph.D. thesis, The Johns Hopkins University, Baltimore, Maryland.

Lämmerzahl P. and 11 colleagues (1987) Expansion velocity and temperatures of gas and ions measured in the coma of Comet P/Halley. *Astron. Astrophys., 187,* 169–173.

Lamy P. L. and Perrin J.-M. (1988) Optical properties of organic grains — Implications for interplanetary and cometary dust. *Icarus, 76,* 100–109.

Larson H. P., Mumma M. J., and Weaver H. A. (1987) Kinematic properties of the neutral gas outflow from Comet P/Halley. *Astron. Astrophys., 187,* 391–397.

Lecacheux, A., Biver N., Crovisier J., Bockelée-Morvan D., Baron P., Booth R. S., Encrenaz P., Florén H.-G., Frisk U., Hjalmarson Å., Kwok S., Mattila K., Nordh L, Olberg M., Olofsson A. O. H., Rickman H., Sandqvist Aa., von Schéele F., Serra G., Torchinsky S., Volk K., and Winnberg A. (2003) Observations of water in comets with Odin. *Astron. Astrophys., 402,* L55–L58.

Marconi M. L. and Mendis D. A. (1983) The atmosphere of a dirty-clathrate cometary nucleus — two-phase, multifluid model. *Astrophys. J., 273,* 381–396.

Markiewicz W. J., Skorov Y. V., Keller H. U., and Kömle N. I. (1998) Evolution of ice surfaces within porous near-surface layers on cometary nuclei. *Planet. Space Sci., 46,* 357–366.

McFadden L. A., A'Hearn M. F., Edsall D. M., Feldman P. D., Roettger E. E., and Butterworth P. S. (1987) Activity of Comet P/Halley 23–25 March, 1986 — IUE observations. *Astron. Astrophys., 187,* 333–338.

Meier R., Eberhardt P., Krankowsky D., and Hodges R. R. (1993) The extended formaldehyde source in Comet P/Halley. *Astron. Astrophys., 277,* 677–690.

Mocknatsche D. O. (1938) *Leningrad State Univ. Annals, Astron. Series Issue 4.*

Morgenthaler J. P., Harris W. M., Scherb F., Anderson C. M., Oliversen R. J., Doane N. E., Combi M. R., Marconi M. L., and Smyth W. H. (2001) Large-aperture [O I] 6300 Å photometry of Comet Hale-Bopp: Implications for the photochemistry of OH. *Astrophys. J., 563,* 451–461.

Morgenthaler J. P., Harris W. M., Scherb F., and Doane N. E. (2002) Velocity resolved observations of H-α emission from Comet Hale-Bopp. *Earth Moon Planets, 90,* 77–87.

Mumma M. J., Weaver H. A., Larson H. P., Davis D. S., and Williams M. (1986) Detection of water vapor in Halley's comet. *Science, 232,* 1523–1528.

Mumma M. J., Weaver H. A., and Larson H. P. (1987) The ortho-para ratio of water vapor in Comet P/Halley. *Astron. Astrophys., 187,* 419–424.

Mumma M. J., McLean I. S., DiSanti M. A., Larkin J. E., Dello Russo N., Magee-Sauer K., Becklin E. E., Bida T., Chaffee F., Conrad A. R., Figer D. F., Gilbert A. M., Graham J. R., Levenson N. A., Novak R. E., Reuter D. C., Teplitz H. I., Wilcox M. I., and Li-Hong X. (2001) A survey of organic volatile species in Comet C/1999 H1 (Lee) using NIRSPEC at the Keck Observatory. *Astrophys. J., 546,* 1183–1193.

Münch G., Hippelein H., Hessmann F., and Gredel R. (1986) *Periodic Comet Halley (1982i).* IAU Circular No. 4183.

Nee J. B. and Lee L. C. (1985) Photodissociation rates of OH, OD, and CN by the interstellar radiation field. *Astrophys. J., 291,* 202–206.

Neufeld D. A., Stauffer J. R., Bergin E. A., Kleiner S. C., Patten B. M., Wang Z., Ashby M. L. N., Chin G., Erickson N. R., Goldsmith P. F., Harwit M., Howe J. E., Koch D. G., Plume R., Schieder R., Snell R. L., Tolls V., Winnewisser G., Zhang Y. F., and Melnick G. J. (2000) Submillimeter wave astronomy satellite observations of water vapor toward Comet C/1999 H1 (Lee). *Astrophys. J. Lett., 539,* L151–L154.

O'Dell C. R., Robinson R. R., Krishna Swamy K. S., McCarthy P. J., and Spinrad H. (1988) C_2 in Comet Halley: Evidence for its being third generation and resolution of the vibrational population discrepancy. *Astrophys. J., 334,* 476–488.

Oliversen R. J., Doane N. E., Scherb F., Harris W. M., and Morgenthaler J. P. (2002) Measurements of C I emission from Comet Hale-Bopp. *Astrophys. J., 581,* 770–775.

Oppenheimer M. and Downey C. J. (1980) The effect of solar-cycle ultraviolet flux variations on cometary gas. *Astrophys. J. Lett., 241,* L123–L127.

Prialnik D., Benkhoff J., and Podolak M. (2004) Modeling the structure and activity of comet nuclei. In *Comets II* (M. C. Festou et al., eds.), this volume. Univ. of Arizona, Tucson.

Richter K., Combi M. R., Keller H. U., and Meier R. R. (2000) Multiple scattering of Hydrogen Ly-alpha: Radiation in the

coma of Comet Hyakutake (C/1996 B2). *Astrophys. J., 531,* 599–611.

Rodgers S. D., Charnley S. B., Huebner W. F., and Boice D. C. (2004) Physical processes and chemical reactions in cometary comae. In *Comets II* (M. C. Festou et al., eds.), this volume. Univ. of Arizona, Tucson.

Scherb F. (1981) Hydrogen production rates from ground-based Fabry-Pérot observations of Comet Kohoutek. *Astrophys. J., 243,* 644–650.

Scherb F., Roesler F. L., Tufte S., and Haffner M. (1996) Fabry-Pérot observations of [O I] 6300, Hα, Hβ and NH_2 emissions from Comet Hyakutake C/1996 B2. *Bull. Am. Astron. Soc., 28,* 927.

Schleicher D. G. and A'Hearn M. F. (1982) OH fluorescence in comets — Fluorescence efficiency of the ultraviolet bands. *Astrophys. J., 258,* 864–877.

Schleicher D. G. and A'Hearn M. F. (1988) The fluorescence of cometary OH. *Astrophys. J., 331,* 1058–1077.

Schleicher D. G. and Farnham T. L. (2004) Photometry and imaging of the coma with narrowband filters. In *Comets II* (M. C. Festou et al., eds.), this volume. Univ. of Arizona, Tucson.

Schleicher D. G., Millis R. L., Thompson D. T., Birch P. V., Martin R. M., Tholen D. J., Piscitelli J. R., Lark N. L., and Hammel H. B. (1990) Periodic variations in the activity of Comet P/Halley during the 1985/1986 apparition. *Astron. J., 100,* 896–912.

Schleicher D. G., Millis R. L., and Birch P. V. (1998) Narrowband photometry of Comet P/Halley: Variation with heliocentric distance, season, and solar phase angle. *Icarus, 132,* 397–417.

Schloerb F. P. (1988) Collisional quenching of cometary emission in the 18 centimeter OH transitions. *Astrophys. J., 332,* 524–530.

Schloerb F. P., Kinzel W. M., Swade D. H., and Irvine W. M. (1987) Observations of HCN in Comet P/Halley. *Astron. Astrophys., 187,* 475–480.

Schloerb F. P., Devries C. H., Lovell A. J., Irvine W. M., Senay M., and Wootten H. A. (1999) Collisional quenching of OH radio emission from Comet Hale-Bopp. *Earth Moon Planets, 78,* 45–51.

Schultz D., Li G. S. H., Scherb F., and Roesler F. L. (1993) The O(^{1}D) distribution of Comet Austin 1989c1 = 1990 V. *Icarus, 101,* 95–107.

Shimizu M. (1976) The structure of cometary atmospheres. *Astrophys. Space Sci., 40,* 149–155.

Skorov Y. V. and Rickman H. (1999) Gas flow and dust acceleration in a cometary Knudsen layer. *Planet. Space Sci., 47,* 935–949.

Skorov Y., Kömle N. I., Keller H. U., Kargle G., and Markiewicz W. J. (2001) A model of heat and mass transfer in a porous cometary nucleus based on a kinetic treatment of mass flow. *Icarus, 153,* 180–196.

Slanger T. G and Black G. (1982) Photodissociation channels at 1216 Å for H_2O, NH_3, and CH_4. *J. Chem. Phys., 77,* 2432–2437.

Smyth W. H., Combi M. R., and Stewart A. I. F. (1991) Analysis of the Pioneer Venus Lyman-α image of the hydrogen coma of Comet P/Halley. *Science, 253,* 1008–1010.

Smyth W. H., Combi M. R., Roesler F. L., and Scherb F. (1995) Observations and analysis of O(^{1}D) and NH_2 line profiles for the coma of Comet P/Halley. *Astrophys. J., 440,* 349–360.

Stephan S. G., Chakrabarti S., Vickers J., Cook T., and Cotton D. (2001) Interplanetary H Ly-α: Observations from a sounding rocket. *Astrophys. J., 559,* 491–500.

Stief L. J., Payne W. A., and Klemm R. B. (1975) A flash photolysis-resonance fluoresccnce study of the formation of O(^{1}D) in the photolysis of water and the reaction of O(^{1}D) with H_2, Ar, and He. *J. Chem. Phys., 62,* 4000–4008.

Tegler S. C., Burke L. F., Wyckoff S., Womack M., Fink U., and DiSanti M. (1992) NH_3 and NH_2 in the coma of Comet Brorsen-Metcalf. *Astrophys. J., 384,* 292–297.

Tozzi G. P., Feldman P. D., and Festou M. C. (1998) Origin and production of C(^{1}D) atoms in cometary comae. *Astron. Astrophys., 330,* 753–763.

van Dishoeck E. F. and Dalgarno A. (1984) The dissociation of OH and OD in comets by solar radiations. *Icarus, 59,* 305–313.

Wallace L. V. and Miller F. D. (1958) Isophote configurations for model comets. *Astron. J., 63,* 213–219.

Wallis M. K. (1982) Dusty gas-dynamics in real comets. In *Comets* (L. L. Wilkening, ed.), pp. 357–369. Univ. of Arizona, Tucson.

Watchorn S., Roesler F. L., Harlander J. M., Jaehnig K. A., Reynolds R. J., and Sanders W. T. (2001) Development of the spatial heterodyne spectrometer for VUV remote sensing of the interstellar medium. In *UV/EUV and Visible Space Instrumentation for Astronomy and Solar Physics* (O. H. Siegmund et al., eds.), pp. 284–295. SPIE Proc. Vol. 4498, SPIE — The International Society for Optical Engineering, Bellingham, Washington.

Weaver H. A., Mumma M. J., and Larson H. P. (1987) Infrared investigation of water in Comet P/Halley. *Astron. Astrophys., 187,* 411–418.

Weaver H. A., Feldman P. D., McPhate J. B., A'Hearn M. F., Arpigny C., and Smith T. E. (1994) Detection of CO Cameron band emission in Comet P/Hartley 2 (1991 XV) with the Hubble Space Telescope. *Astrophys. J., 422,* 374–380.

Weaver H. A., Feldman P. D., A'Hearn M. F., Arpigny C., Brandt J. C., and Stern S. A. (1999) Post-perihelion HST observations of Comet Hale-Bopp (C/1995 O1). *Icarus, 141,* 1–12.

Weaver H. A., Feldman P. D., Combi M. R., Krasnopolsky V., Lisse C. M., and Shemansky D. E. (2002) A search for argon and O VI in three comets using the Far Ultraviolet Spectroscopic Explorer. *Astrophys. J. Lett., 576,* L95–L98.

Womack M., Festou M. C., and Stern S. A. (1997) The heliocentric evolution of key species in the distantly-active Comet C/1995 O1 (Hale-Bopp). *Astron. J., 114,* 2789–2795.

Wu C. Y. R. and Chen F. Z. (1993) Velocity distributions of hydrogen atoms and hydroxyl radicals produced through solar photodissociation of water. *J. Geophys. Res., 98,* 7415–7435.

Wyckoff S., Tegler S., Wehinger P. A., Spinrad H., and Belton M. J. S. (1988) Abundances in Comet Halley at the time of the spacecraft encounters. *Astrophys. J., 325,* 927–938.

Xie X. and Mumma M. J. (1996a) Monte Carlo simulation of cometary atmospheres: Application to Comet P/Halley at the time of the Giotto spacecraft encounter. I. Isotropic model. *Astrophys. J., 464,* 442–456.

Xie X. and Mumma M. J. (1996b) Monte Carlo simulation of cometary atmospheres: Application to Comet P/Halley at the time of the Giotto spacecraft encounter. II. Axisymmetric model. *Astrophys. J., 464,* 457–475.

Yamamota T. (1981) On the photochemical formation of CN, C_2 and C_3 radicals in cometary comae. *Moon and Planets, 24,* 453–463.

Yamamota T. (1985) Formation environment of cometary nuclei in the primordial solar nebula. *Astron. Astrophys., 142,* 31–36.